

**THE USE OF 3D-PRINTED PHANTOMS
FOR EVALUTING CT IMAGE QUALITY**

by

Hui Shi

A thesis submitted to Johns Hopkins University in conformity with the requirements for
the Degree of Master of Science in Engineering

Baltimore, Maryland
December 2019

© 2019 HUI SHI

All right reserved

ABSTRACT

This thesis is about applying 3D printing in evaluating CT image quality and showing how this low-cost and fast-prototyping technique has the potential to create a paradigm shift in phantom design from simple geometrical objects to more sophisticated structures that incorporate anatomical features. Phantoms are used as surrogates for humans when evaluating the performance of CT imaging systems, but traditional molding techniques limit phantom designs in rigidly defined size, geometry, and material composition. Conventional phantoms are able to quantitatively evaluate the imaging system, but they overlook the complexity of the structural and textural properties of human anatomy. The high cost of the phantoms also limits the feasibility of customization and patient-specific individualization. CT image quality is highly dependent on various factors, such as the object's size, geometry, the reconstruction method, and the image post-processing. Due to the object-dependence of CT image quality, it is important to evaluate on realistic objects. The anthropomorphic phantoms with known texture features are therefore needed to quantitative evaluate CT system. To this end, we utilize the recently emerged 3D-printing technology for constructing low-cost anthropomorphic phantoms. We devise a methodology for 3D-printed phantom inserts that represent the structural and textural properties that may be placed inside a large anthropomorphic phantom to simulate the bulk properties of the human body. We expect that this general method can be used as a repeatable and robust imaging performance assessment methodology that includes quantitative analysis of the reconstruction of specific textures and anthropomorphic features.

Thesis Committee Members

J. Webster Stayman, Ph.D. (Primary Advisor)

Associate Professor, Department of Biomedical Engineering

Johns Hopkins University

Wojtek Zbijewski, Ph.D.

Assistant Professor, Department of Biomedical Engineering

Johns Hopkins University

Grace J. Gang, Ph.D.

Assistant Research Professor, Department of Biomedical Engineering

Johns Hopkins University

TABLE OF CONTENTS

	Page
ABSTRACT	ii
LIST OF TABLES	vii
LIST OF FIGURES	viii
LIST OF SYMBOLS AND ABBREVIATIONS	ix
ACKNOWLEDGEMENTS	x

CHAPTER

1	Introduction to CT Imaging Systems	
1.1	General Introduction	1
1.2	X-ray Generation	3
1.3	X-ray Attenuation and Interaction with Matter	4
1.4	Solid-State X-ray Detection	7
1.5	Traditional CT Reconstruction	7
1.6	Advanced reconstruction methods in X-ray CT	11
2	Image Quality Assessment	
2.1	Traditional Performance Parameter of the CT scanner	13
2.2	High-contrast Spatial Resolution	14
2.3	Noise Measurement	16
2.4	Texture Characterization of CT Images	17
3	The Use of Phantoms for Evaluating CT Systems	
3.1	Introduction to Imaging Phantoms and Three-dimensional Printing	19
3.2	Traditional Imaging Phantoms	20

3.3 Introduction to Rapid Prototyping and Manufacturing	22
3.4 A Modular Liver Anthropomorphic Phantom	24
3.4.1 Creating the Molding Framework	25
3.4.2 Silicon Room Temperature Vulcanizing (RTV) Molding	25
3.4.3 Resin Casting of the Abdomen Phantom	27
3.5 Fabrication of Quantifiable Texture Phantom Inserts	28
3.5.1 Generating Spheres	29
3.5.2 Compiling the Spheres and the Texture Phantom Body	30
3.5.3 Generating Print Support	31
3.5.4 Stereolithography Process	32
3.6 Investigation of the K_2HPO_4 Concentration vs. CT Contrast	34
3.7 Combining Elements into a Modular Texture Insert	35
4 Performance Assessment of Texture Reproduction	
4.1 Method	38
4.1.1 Phantom Scanning	38
4.1.2 Computation of Radiomics Features	39
4.2 Results	40
4.3 Discussion and Future Work	46
5 Vascular Stenotic Phantom Insert as Performance Metric	
5.1 Morphological Patterns	47
5.2 Design and 3D-print the Vascular Phantom	
5.2.1 Vascular Stenotic Phantom Insert as the Performance	47
Phantom	
5.2.2 Design and 3D-print of the Vascular Phantom	48
5.2.3 Discussion and Future Work	51

5.3 Annular Phantom	
5.3.1 Clinical Implications	52
5.3.2 Computer-aided Design of the Annular Phantoms	52
5.3.3 CT Scans of the Annular Phantoms	54
5.3.4 Estimating Edge Sharpness	55
5.3.5 Results	56
5.4 Spiculated Phantom	
5.4.1 Clinical Significance of the Spiculated Phantom	60
5.4.2 Design of the Spiculated Phantoms	60
5.4.3 CT Scan of the Spiculated Phantoms	61
5.5 Discussion and Future Work	62
REFERENCES	63
CV	68

LIST OF TABLES

	Page
Table 1. Setting for the CURA	32
Table 2. Summary of the Range of Diameters of the Hollow Cylinders	49

LIST OF FIGURES

	Page
Figure 1: The different CT Imaging modalities	2
Figure 2: X-ray Tube	4
Figure 3: The Mechanisms of X-ray Interaction with Biological Tissue	6
Figure 4: Parallel Beam Schematic	8
Figure 5: Ramp Filter Can Eliminate Blurring Effects in the Back-projection in the CT Reconstruction	9
Figure 6 Coronal CT-scan of patient with multiple liver tumors (UCSF)	17
Figure 7: Image Assessment Phantom	21
Figure 8: Multipurpose Chest Phantom Kyoto Kagaku N1 "LUNGMAN"	22
Figure 9: Essential Materials Used to Cast the Anthropomorphic Phantom.	24
Figure 10 RTV molding process	26
Figure 11. Abdomen Cast	27
Figure 12. Overall Process for Creating Texture Phantom	28
Figure 13. Example of the Conglomeration of Spheres within the Confined Cylindrical Volume	29
Figure 14. The Texture Phantom	30
Figure 15. The Texture Phantom with Support	31
Figure 16. Printer and Print Objects	33
Figure 17. Correlation of Concentration and Hounsfield value.	34
Figure 18. Lining up the texture phantoms together with spacing between each other	36
Figure 19. Contrast Enhanced Texture Phantom	36
Figure 20. Texture Performance Assessment under Realistic Condition	37

Figure 21. Illustration of the Four GLCM Offset Direction Used	39
Figure 22. Qualitative Comparison of Texture Phantom Scans	41
Figure 23. A Summary of GLCM Features	42
Figure 24. Plots of GLCM-Correlation Minimum for Different Modalities as a Function of Feature Size	43
Figure 25. GLCM-Correlation and GLCM-Homogeneity for the Heterogeneous Inserts	44
Figure 26. The GLCM Features with the added Anthropomorphic Data Set	45
Figure 27. Liver Lesion with Iodine Enhancement from the Rabbit Model	46
Figure 28. Schematic illustration of the stenotic phantom	50
Figure 29. 3D Printed Stentoic Phantom	50
Figure 30. CT scan of the phantoms	51
Figure 31. Schematics of the Annular Phantom Design	52
Figure 32. Schematics Diagram Showing how the Phantoms are Filled	54
Figure 33. Annular Phantoms with Contrast	57
Figure 34. Box Plots of the Modeling Result	59
Figure 35. Patterns of Margin	60
Figure 36. Schematics of the Design of the Spiculated Phantom	60
Figure 37. Parameters for the Specific Design	61
Figure 38. CT images of the Spiculated Phantom	62

LIST OF SYMBOLS AND ABBREVIATIONS

Abbreviation	Name
CT	Computed Tomography
HU	Hounsfield Unit
PL	Penalized Likelihood
MTF	Modulation Transfer Function
NPS	Noise Power Spectrum
LP	Line Pair
ROI	Region of Interest
CT	Computed Tomography
GLCM	Gray Level Co-occurrence Matrix
3D	Three Dimensional
RP&M	Rapid Prototyping and Manufacturing
RTV	Room Temperature Vulcanizing
CNC	Computer Numerical Control
STL	Standard Tessellation Language
CAD	Computer Aided Design
HRCT	High Resolution Computed Tomography
NRCT	Normal Resolution Computed Tomography
HRCE - CT	High Resolution Contrast Enhanced Computed Tomography
NRCE - CT	Normal Resolution Contrast Enhanced Computed Tomography

ACKNOWLEDGEMENT

I am thankful to my advisor Dr. Joseph Webster Stayman, who gave me the opportunity to embark on medical imaging and explore the physics, engineering and design of the computerized tomography and its computational and physical tools. Web's astute research vision, broad physical science knowledge, and commitment to research have motivated me to develop focus and resilience in the problem-solving process. His patience and insightful instructions always help me overcome the bottlenecks during the problem-solving process.

I would like to thank my peers and colleagues in the AIAI and ISTAR lab - here they are in no particular order except alphabetical - Qian Cao, Jessica Flores, Michael Kecha, Junyuan Li, Andrew Leong, Shaoyan Pan, Gabriela Rodal, Niral Sheth, Gengxin Shi, Alejandro Sisniega, Matthew Tivnan, Steven Tilley, Wenyi Wang, Pengwei Wu, and Hao Zhang. I am grateful to them all, and I acknowledge their helpful advice and jocular quips during this painfully creative research process. I am especially grateful to those who gave their precious time to exchange ideas and suggest ways of improvements. I am also grateful to Dr. Zbijewski and Dr. Gang for supporting my research and serve as my thesis committee.

Finally, I would like to thank my parents and my friends for their moral support. You are the people who lift me up and make my Master's degree experience memorable.

CHAPTER 1

INTRODUCTION TO CT IMAGING SYSTEM

1.1 General Introduction

Computerized Tomography (CT) is a digital modality of medical imaging that allows the user to view orthogonal planes (e.g. coronal, sagittal and axial) or cross-section through the human body. By taking advantage of tissues' varying attenuation of x-rays, CT uses x-rays at different projection angles to form a 3D image volume. High-quality CT images reveal valuable diagnostic information and have become an important investigative tool in the clinical practice - playing a key role in diagnosing and locating tumor sites, examining internal injury or trauma, guiding surgical procedures, pinpointing biopsy sites, detecting abnormal blood vessels or fractured bones, and many other abnormalities. Quantitative image quality assessment of the CT systems is indispensable for understanding the diagnostic capacity of the CT system.

Higher x-ray exposures improve image quality by decreasing quantum noise. However, increased x-ray exposure increases patient risks due to DNA damage from ionizing radiation. Thus, image quality is often limited by x-ray dosage. Because of the tradeoff between image quality and x-ray exposure, it is important to understand the diagnostic strength of the CT system in screening diseases at a safe dose level. This process is known as image quality assessment, which comprises testing of image contrast, noise, and resolution through quantitative measurements.

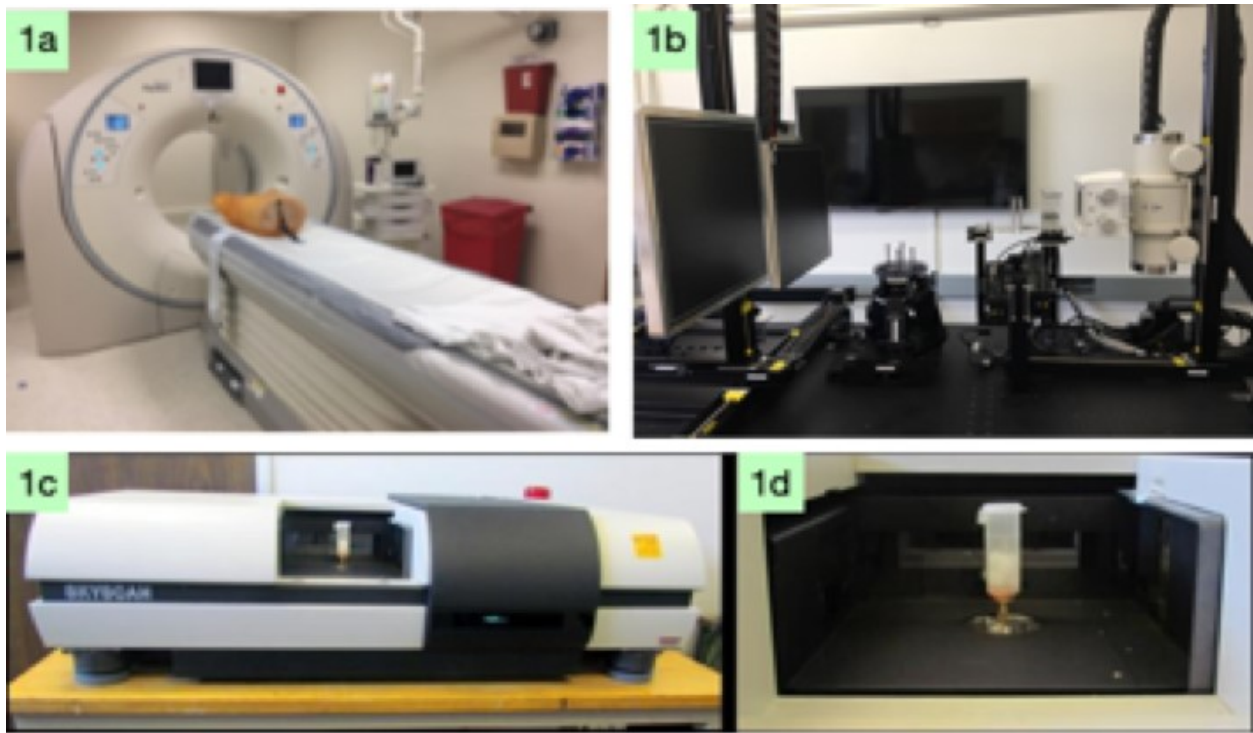


Figure 1. The different CT Imaging modalities: 1a. helical CT system. 1b. experimental benchtop cone beam CT system. 1c-d. micro-CT system: 1c – the overall machine; 1d – the internal chamber of the micro-CT system for placing the scanned object (Peteya, 2013)

Many CT systems with different acquisition procedures have emerged in routine clinical practice for different diagnostic purposes. Different CT systems have their own strengths and weaknesses and are often complementary to each other. In this work, we would like to introduce the two commonly used medical CT systems (helical CT and cone-beam CT) as well as a micro-CT system. Helical CT (Figure 1a) is the most widely used method for its fast scan time, which increases efficiency and reduces motion artifacts from patients. “Helical” refers to the data acquisition where the images are obtained in a spiral trajectory by moving a still patient on a scanning table at a constant speed into a slip-ring gantry with continuously rotating x-ray tubes and detectors. Because of its efficiency, it is widely used in disease screening and follow-up. (Zeman et. al., 1993) Cone-beam CT (Figure 1b) does not require patients to be moved and often provides higher resolution images. “Cone beam” refers to the relatively large x-ray beam

coverage enabled by a large-area flat panel detector. In this case, the volume may be covered by a single circular rotation with the detector on one side and the x-ray tube on the other side revolving around the patient (Miracle et. al., 2009). Such systems are usually less expensive than helical CT and are deployed, for example, in guiding surgery in the operating room and visualizing bony structure in the head. Micro-CT (Figure 1c-d) is another type of CT imaging modality that scans smaller scale objects like tissue biopsies (Ritman, 2004). As the name suggests, Micro-CT renders an image with very fine resolution. We will use such scan to serve as the ground truth in our investigation.

1.2 X-ray Generation

X-rays are electromagnetic waves with short wavelength and relatively high photon energy. X-rays are invisible to the eye, highly penetrable, and travel at the speed of light. Traditional x-rays generation is through the collision of fast-moving electrons and an anode target. An x-ray tube (figure 2), along with a high voltage generator and controller, forms the x-rays generator in a CT system. The voltage generator provides the voltage differentials between the cathode and anode. The controller is a platform to command the x-ray tube settings such as mA, kVp, and exposure time explicitly. The x-ray tube is a vacuumed space shielded inside a glass housing to eliminate the friction for the high-speed electrons and to protect the cathode filament from being oxidized. Inside the evacuated space there is a cathode filament that supplies electrons and an anode target where the collision happens. The cathode filament, often made of tungsten, can be heated to generate a stream of electrons. When the voltage is constant, the higher current (mA) induces higher temperature in the cathode filament, which emits more

electrons. For modular CT tubes, the anode target is typically a revolving disc made of tungsten, heat-tolerant target, and a copper core/base to conduct and release heat. When a high voltage is applied between the cathode and the anode, the electrons on the cathode side speed up towards the anode side and collide into the anode target, converting the kinetic energy into other forms of energy, where categorically 99% dissipated as heat and the rest the desired x-ray radiation. The majority of the x-ray radiation is known as the bremsstrahlung radiation, meaning braking radiation in German. (Hsieh, 2015)

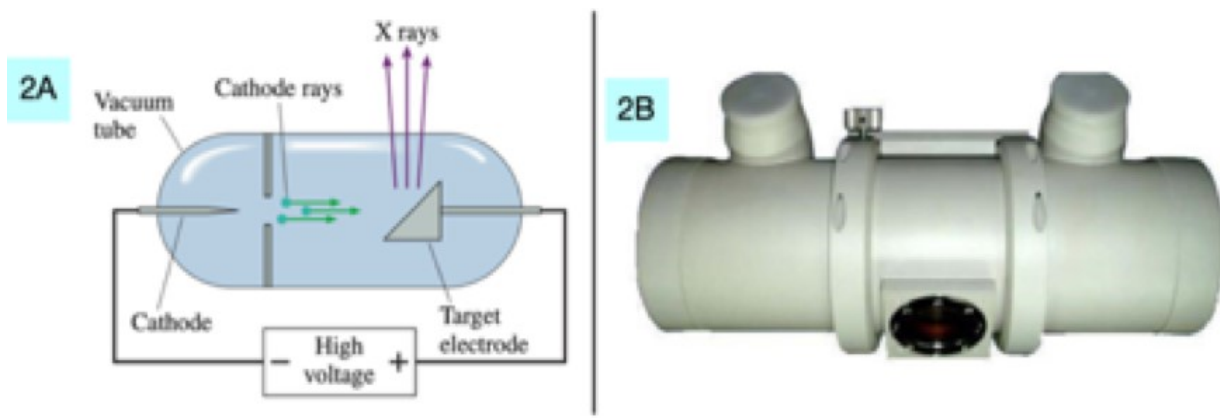


Figure 2. X-ray tube. 2A. Schematic diagram of the x-ray tube (Randall, 2015). 2B. Actual x-ray tube

1.3 X-rays Attenuation and Interaction with Matters

X-rays interact with matter at the atomic level. Because the high energy carried by x-rays exceeds the binding energy of the electrons, the interaction between the x-ray photon and the atom can produce free electrons (also known as photoelectrons) and secondary radiation source such as the characteristic radiation. The free electrons and the secondary radiation source continue interacting with the surrounding atoms. Compared to the x-ray photons, these photoelectrons have more hazardous effect in the biological system. Unlike the x-ray photons

releasing most of the energy in one interaction, the electrons releasing small amounts of energy in each interaction gradually exhaust their energy through many interactions. In addition, since photoelectrons are negatively charged, they can ionize the other electrons in the vicinity without direct contact, resulting in a larger scale of direct DNA damage. Although it is well known that x-rays photons are carcinogenic, it is the heavier charged byproduct of x-ray photons that is the prime culprit for DNA damage.

In medical diagnostic procedures, x-rays interact with the human body via two primary mechanisms: photoelectric absorption and Compton scattering. Photoelectric absorption refers to the process where the x-ray photon transfers all the energy to an electron in the lower atomic shell, producing a free-electron carrying kinetic energy and characteristic radiation from the higher shell electron filling in the empty shell. The characteristic radiations of the human tissues are low energy and the human body completely absorbs them. Photoelectric absorption generates desirable signals that show how the x-rays get attenuated by different tissues and, thus, carries valuable information about tissue properties. However, patients receive ionization from this process. Compton scattering refers to the process where the photon collides with the electron resulting in changed trajectories for both the electron and the photon. This effect is undesirable because the scattered x-rays add noise to the primary attenuated x-ray signal in the projection image and reduce image contrast. The probabilities of occurrence for both photoelectric absorption and Compton scattering are inversely proportional to the energy of the x-rays where the Compton scattering ($P(\text{Compton}) \propto \frac{Z}{h\nu}$, where Z is the atomic number, $h\nu$ is the photon energy) is more sensitive to high energy x-ray than the photoelectric absorption($P(\text{photoelectric}) \propto \frac{Z^4}{h\nu^3}$). In addition to the signal differences provided by tissues, contrast agents such as iodine or barium with high atomic number and many layers of atomic

shell are used. The contrast agents can induce photoelectric absorption and the secondary characteristic radiations generated through the photoelectric absorption can penetrate through the body and contribute to the imaging signals, creating better contrast to show the visibility of the organ that encapsulates them.

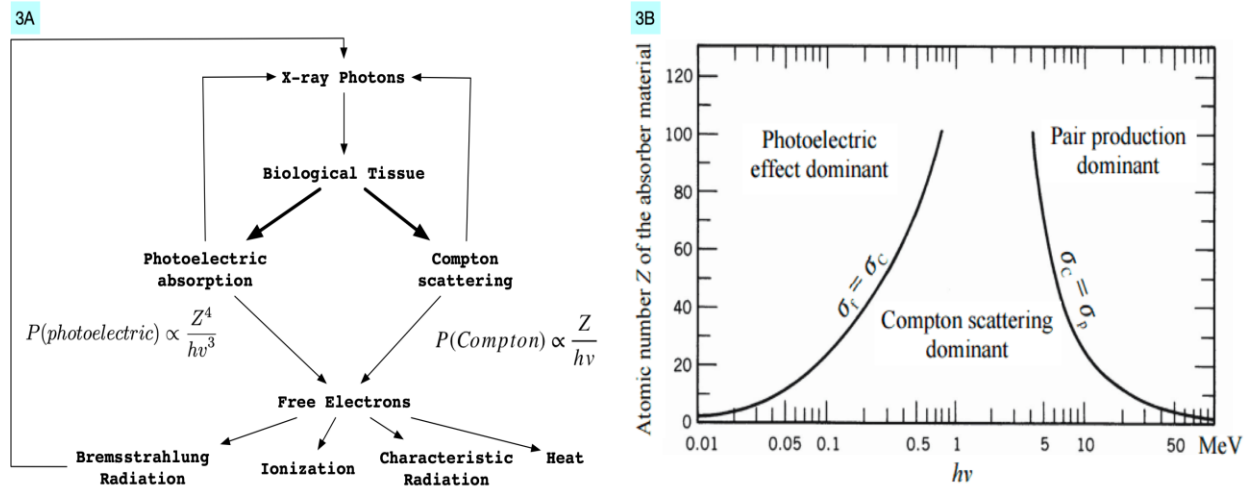


Figure 3. The mechanisms of x-ray interaction with biological tissue. 3A - a schematic diagram of the interaction. 3B - phase diagram of different effect (University of Wisconsin, 2019).

Several factors such as the material thickness and the tissue properties contribute to the attenuation of X-rays. These can be expressed mathematically by the Beer-Lambert law, which relates the attenuation of the incident x-rays to the properties of the absorber. Specifically, the attenuated x-ray intensity(I) may be described as:

$$I(z) = I_0 e^{-[\frac{\mu}{\rho}] \rho z}$$

where I_0 is the incident x-ray intensity, $\frac{\mu}{\rho}$ is the mass attenuation coefficient, ρ is the density of the material, and z is the length of the x-ray path.

The amount of attenuation through the absorber is determined by the incident x-rays' beam energy(kVp) and the absorber's material properties such as the atomic number, density, and electrons per gram. Generally, the higher the beam energy, the more penetrable the x-rays.

X-rays are more attenuated in an absorber with a higher atomic number because of the positive correlation between the atomic number and the probability of photoelectric absorption and Compton scattering (Figure 3). Thirdly, x-rays are more attenuated going through denser tissue or tissue with more electrons in its atomic shell. (Hsieh, 2015)

1.4 Solid-State X-Ray Detector

Unattenuated x-rays arrive at the x-ray detector, which is comprised of a set of photodiodes and small blocks of scintillating materials such as CsI , Gd_2O_2S , HiLightTM or GEMS StoneTM. X-ray photons undergo photoelectric absorption with the scintillators generating characteristic radiation. These visible light photons are focused by reflective materials towards the photodiodes at the bottom of the detectors to produce electrical signals. The electrical signals are converted to digital numbers which collectively form a projection image. (Hsieh, 2015)

1.5 CT Reconstruction

A CT system takes multiple projections of an object at different angles and estimates the attenuation distribution within a volume. This estimation process is called reconstruction. The reconstruction algorithm relies on a mathematical definition of the geometry of the scanner. Different geometries include cone-beam, parallel-beam, fan-beam, and helical systems. A parallel beam geometry is illustrated in figure 4, where the projection of the object is the line integral of the object's intensity at an angle. One pivotal theorem for deriving the intensity of the

object based on the projection images is the Fourier slice theorem, which relates 2D Fourier transform of the object to 1D Fourier transform of its projections.

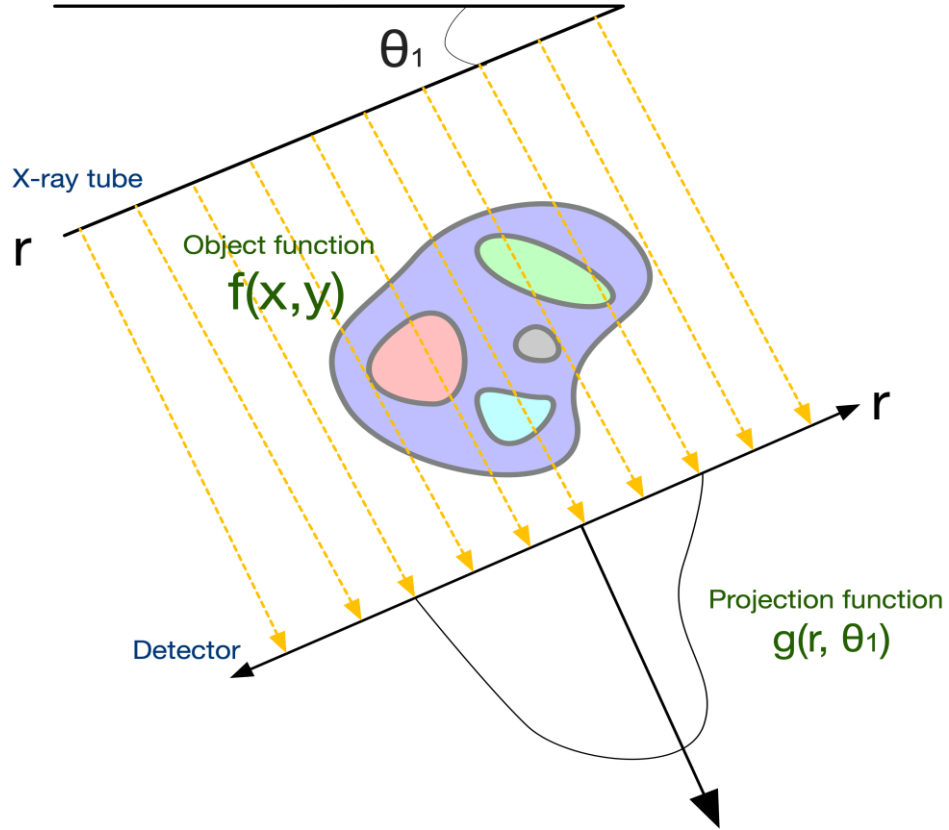


Figure 4. Parallel Beam Schematic. The angle between the horizontal line x and the projection line r is θ_1 . The projection function is the line integral of the attenuation coefficient of the object function. Physically, it represents the attenuated x-rays' intensity. For a fixed θ , $g(r, \theta_1)$ is a projection, which is the line integral onto the projection line. For all the projections, $g(r, \theta_1)$ is the sinogram, or the 2D radon transform of the object.

To derive the Fourier slice theorem, recall the 2D Forward Fourier transform and its inverse:

$$\text{Forward Fourier transform: } F(u, v) = \int_{-\infty}^{\infty} \int_{-\infty}^{\infty} f(x, y) e^{-j2\pi(ux+uy)} dx dy$$

$$\text{Inverse Fourier transform: } F(u, v) = \int_{-\infty}^{\infty} \int_{-\infty}^{\infty} f(u, v) e^{j2\pi(ux+uy)} du dv$$

The sinogram is

$$g(r, \theta) = \int_{-\infty}^{\infty} \int_{-\infty}^{\infty} f(x, y) \delta(x \cos \theta + y \sin \theta - r) dx dy$$

The Fourier Transform of the sinogram is:

$$G(q, \theta) = \int_{-\infty}^{\infty} g(r, \theta) e^{-j2\pi qr} dr$$

Substituting $g(r, \theta)$ into $G(q, \theta)$:

$$\begin{aligned} G(q, \theta) &= \int_{-\infty}^{\infty} \int_{-\infty}^{\infty} \int_{-\infty}^{\infty} f(x, y) \delta(x \cos \theta + y \sin \theta - r) e^{-j2\pi qr} dx dy dr \\ &= \int_{-\infty}^{\infty} \int_{-\infty}^{\infty} f(x, y) e^{-j2\pi q(x \cos \theta + y \cos \theta)} dx dy \end{aligned}$$

The 2D Fourier transform of $F(u, v) = \int_{-\infty}^{\infty} \int_{-\infty}^{\infty} f(x, y) e^{-j2\pi(ux+vy)} dx dy$

Apparently, when $u = q \cos \theta, v = q \sin \theta,$

$$G(q, \theta) = F(u, v)$$

The Fourier slice theorem, also known as the projection slice theorem, states that the Fourier transform of the projection of an object directly gives the values in the Fourier domain representation of the object. Specifically, the Fourier transform of each projection is a line in the Fourier transform of the object. Thus, collecting enough projections allows one to fill in the entire Fourier space of the object. The object attenuation distribution could then be recovered by taking the inverse Fourier transform. This theorem alone presents several challenges for image reconstruction. The discrepancy in polar coordinate sampling in the Fourier space and cartesian coordinate sampling contributes to interpolation errors.

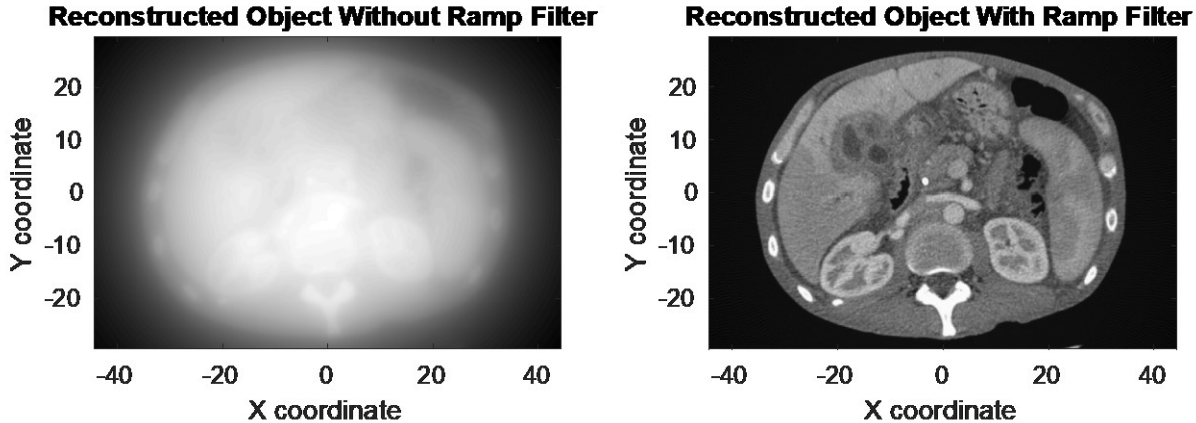


Figure 5. Ramp Filter Can Eliminate Blurring Effects in the Back-projection in the CT reconstruction. Left: simulated reconstruction object without ramp filter; Right: simulated reconstruction with ramp filter (Ali, 2016)

Alternately, one can perform reconstructions via back-projection - in effect “smearing” measurement varies back into the image volume. While pure back projection forms an image similar to the object, it is blurry. This is because the response of the projection then back-projection is a strong ($\frac{1}{r}$) radial blur. To resolve this blur, we can apply a high frequency filter before the back-projection. One can show that a ramp filter applies to projection data will eliminate the $\frac{1}{r}$ blur. This reconstruction method is generally referred to as filter-back projection (FBP).

In order to compare data from the different scanners with various energy settings and X-ray sources, we can compute the normalized value of the x-ray absorption coefficient of each voxel in a CT image. This number is known as the CT number is expressed in Hounsfield unit (HU). Mathematically it is defined as:

$$h = 1000 \times \frac{\mu - \mu_{water}}{\mu_{water}}$$

where μ is the linear attenuation coefficient of the material. (Prince, 2015)

1.6 Advanced reconstruction methods in X-ray CT

With the availability of faster computational power and iterative reconstruction (IR) algorithms have been widely developed by major CT vendors for their noise reduction capacity. These methods go beyond filtered back projection to maintain or improve image quality while substantially reducing x-ray exposure to patients. While IR has become widespread and is generally viewed as having improved image quality, the image properties produced by such algorithms are often much more complex than FBP-type approaches.

Iterative reconstruction starts with an initial volume estimate – e.g. an all zero/ “empty” image or a filtered back projection reconstruction. The difference between the re-projected current image estimate and the measured raw data gives us a correction term, which maybe back projected onto the volumetric object estimate. The iteration process ends when either a fixed number of iterations or the image quality criterion is reached. (Beister, 2012)

Penalized-likelihood (PL) iterative reconstruction is one of many possible model-based reconstruction techniques. The forward model in matrix form can be expressed as:

$$\bar{y} = \mathbf{D}\{g\}exp(-l), l = \mathbf{A}\mu$$

where the mean measurements \bar{y} are a function of the measurement dependent gains (g) multiplied by the exponential form of the negative line integral ($-l$) of the image volume.

The objective function for PL estimation is:

$$y = \underset{\mu}{\operatorname{argmax}} \log L(y; \mu) - R(\mu; \delta) = \underset{\mu}{\operatorname{argmax}} \sum_{i=1}^N h_i(l_i) - \beta_R \|\Psi_R \mu\|_{p_R}^{p_R}$$

where $h_i(l_i)$ is the marginal log-likelihood for each measurement and can be expressed as:

$$h_i(l_i) = \sum_{i=1}^N y_i \log(g_i \exp(-l_i)) - g_i \exp(-l_i)$$

Here, $R(\mu; \delta)$ is an arbitrary regularizer, β_R is the scalar control parameter allowing us to fine tune the estimator for specific noise-resolution trade-off, and Ψ_R is a sparsifying operator (e.g. a finite differencing matrix). (Stayman et.al., 2013)

The relationship between regularization strategies and specific β_R values is often complex with no explicit closed form expression for, e.g., spatial resolution. Moreover, the noise and resolution of the image is typically space-variant/non-stationary and can depend on the patient size and anatomy. Increasingly sophisticated regularization methods can have more data dependence – enhancing edges and smoothing features interpreted as noise. This can have impact on anatomical features if the regularization is not tuned properly or is too aggressive in noise reduction.

In recent years, machine learning methods have increasingly been investigated and starting to find their way into clinical systems. Such data-driven approaches have the potential for improved image quality over IR but are likely to exhibit even greater object-dependence. For both IR and machine learning, these dependencies made quantitative image-quality analysis even more complex.

CHAPTER 2

IMAGE QUALITY ASSESSMENT

2.1 Traditional Performance Parameters of the CT scanner

The ability of a CT system to render fine details and differentiate low-contrast objects from background is critical for accurate clinical detection and diagnosis. Image quality is determined by several factors such as scanner characteristics (detector performance, scan speed, sampling, etc.), x-ray exposure and technique, properties, and reconstruction parameters. Discrepancies always exist between the “true” object and the image estimate. CT image quality can be broken down into different characteristics including resolution, contrast, noise, and artifacts. These characteristics are often coupled – e.g. finer resolutions can be achieved but with increased noise. Thus, in order to make well-informed decisions in specifying acquisition of reconstruction protocols for different diagnostic purposes, it is important to be able to characterize the performance attributes across protocols. In the following sections, we will review some common practices for evaluating the CT systems. These includes high-contrast spatial resolution measurements, the modulation transfer function (MTF), noise measurement including noise power spectrum (NPS), and mixed measures line signal to noise ratio (SNR).

2.2 High-contrast Spatial Resolution

High-contrast spatial resolution is a measurement of the ability of an imaging system to render the object details and to identify or distinguish small and closely spaced features. CT spatial resolution is often characterized by scanning a thin tungsten wire or line pair gauge. The line pair gauge is a series of parallel line bars whose size and spacing can be used to probe specific spatial frequencies. The spatial resolution can be subjectively measured by maximum spatial frequency line pair where the eye is able to distinguish the individual line pairs. To express the resolution in terms of these line pair we use the unit line pair per millimeter (LP/pixel).

Alternatively, another quantitative resolution measure is the modulation transfer function (MTF), which shows how the contrast is reproduced in a system as a function of spatial frequency. To understand MTF we must start with the concept of modulation. The signal modulation is the contrast between the bright and dark regions of the image and is defined as

$$M = \frac{A_{max} - A_{min}}{A_{max} + A_{min}} = \frac{ac}{dc}$$

where A represents the amplitude of the signal. The ratio of image modulation to the object modulation is the modulation transfer ratio; that is,

$$MT(\xi) = \frac{M_{image}(\xi)}{M_{object}(\xi)}$$

where ξ is the spatial frequency. The modulation transfer ratio shows the amount of details preserved in the imaging system. Characterizing the system behavior at a specific spatial frequency. To describe the full system response, we can plot the MTF, which characterizes how the modulation transfer ratio changes across all spatial frequencies. MTF generally decreases at higher spatial frequency, where the scale of details is smaller.

One resolution limit in any imaging system is tied to sampling (e.g. pixel value). The Nyquist-Shannon sampling theorem states that to preserve a continuous time signal, the minimum uniform sampling frequency f_s must be twice the maximum frequency component f_{max} Hz of the continuous signal; i.e., $f_s \geq 2f_{max}$. This means that the detector will not register frequency components of the object greater than one half of its sampling frequency (i.e. the Nyquist frequency). When the sampling frequency is less than the Nyquist frequency, the signal will get aliased and the details will not be preserved. With regard to MTF, both pre- and post-sampling MTFs are often reported. The post-sampling MTF is naturally limited to frequencies below Nyquist.

MTF can be characterized as the modulus of the Fourier transform of the linear spread function (LSF) at a specific direction, which, in turn, is related to the derivative of the edge spread function. Specifically,

$$\begin{aligned} MTF(v) &= |\mathcal{F}\{LSF(x)\}| \\ &= |\mathcal{F}\left\{\frac{d}{dx}[ESF(x)]dx\right\}| \\ &= \frac{1}{\sqrt{2\pi}} \int_{-\infty}^{\infty} \frac{d}{dx}[ESF(x)] e^{i2\pi vx} dx \end{aligned}$$

where v is the spatial frequency, x is the spatial distance, and \mathcal{F} represent the Fourier transform.

The MTF characterizes the contrast degradations of the CT system in terms of spatial frequency, which presumes that the resolution properties are space invariant. However, this assumption is often not true. For example, variations caused by the apparent focal spot shape as the detector angle changes and nonuniform spatial sampling patterns as the distance to iso-center changes can lead to space variant behavior. Moreover, nonlinear data processing methods and advanced regularization can similarly lead to space-variant effects (Hsieh, 2015)

2.3 Noise Measurement

Noise is random fluctuation of an otherwise uniform image resulted by the x-ray quantum noise, inherent noise of the CT system, and often potential stochastic elements of the image generation process. Quantum Noise is tied to the x-ray exposure, which is limited to ensure patient safety. Though variance can represent the level of noise in an image, noise power spectrum (NPS) is a more comprehensive noise descriptor. The NPS describes the noise at each spatial frequency, and is useful for prediction of detection performance (Baek et.al., 2010).

The local noise power spectrum is obtained by squaring the magnitude of the fourier transform of the noise image; that is

$$NPS(u, v) = \frac{1}{A} \langle \left| \iint_A n(x, y) e^{-2\pi i(xu+yv)} dx dy \right|^2 \rangle$$

where $n(x, y)$ is the reconstructed image containing only noise, u and v are frequency variables, and A represents the area over which $n(x, y)$ is defined.

Although NPS is a standard practice for image noise assessment, it is limited to images with wide-sense stationary noise; that is, the image whose statistics are constant throughout the entire image. Tools have been developed to select the local region of interest (ROI) to compute the NPS, but studies have shown that the NPS is dependent on the choice of various factors as the ROI size decreases. These factors include the choice of background removal and window function. These dependencies may affect the interpretations of NPS for task-based image quality assessment and therefore need to be understood. (Barrett, 2018)

2.4 Texture Characterization of CT Image and GLCM

Traditional performance parameters (like MTF and NPS) are able to give a broad overview of the scanner capability, but they do not generally take diagnostic task into account. Moreover, with the knowledge of tumor signatures becoming more comprehensive (e.g. radiomics) and treatment plans more individualized, radiologists develop more sophisticated methods to characterize the tumor in the CT image for better prognosis and treatment plans. Tumors are often spatially heterogeneous on the gross and cellular levels, where the more heterogeneous tumor tends to be linked to more malignant lesions. Therefore, texture can be used as a biomarker for tumor detection or benign/malignant tumor differentiation. CT textures analysis has the potential to use quantitative imaging features of tumor texture to diagnose and stage cancer. Texture analysis provides an objective assessment of the tumor heterogeneity by analyzing the voxel distributions of the lesion. In addition, these extraction and classification methods of the CT textures can be used as a virtual biopsy for the indeterminate masses and can improve prognosis and treatment methods.

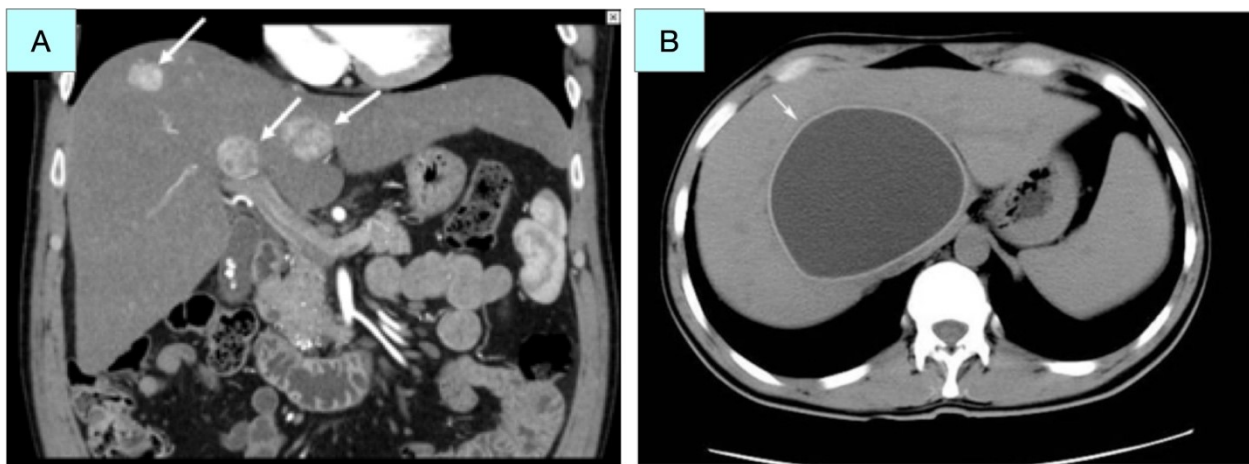


Figure 6. Illustration of CT images; A- Coronal CT-scan of Patient with Multiple Liver Tumors, where the shape is nonuniform and the texture is inhomogeneous (UCSF,2019); B-Axial CT-scan of Patient with Cyst, where the shape is rounded, and the texture is uniformly distributed (Yuksel et.al., 2007);

One common way to summarize the texture of an image is the gray level concurrence matrix (GLCM). As its name suggests, GLCM represents the distribution of co-occurring voxel grayscale values from the gray-scale value of another pixel at a given offset. The matrix represents how often a pixel with gray-level value i occurs to adjacent pixels with value j with different offset directions and distances. The offset direction can be chosen arbitrarily, e.g. - horizontally, vertically or diagonally. After creating the GLCM, one can derive several classes of statistics such as homogeneity and correlation to characterize the texture of an image.

Homogeneity is the value that measures the closeness of the distribution of elements in the GLCM to the GLCM diagonal; that is:

$$\text{Homogeneity} = \sum_{i,j=0}^{N-1} \frac{P_{ij}}{1+|i-j|}$$

Where P_{ij} is the element i, j of the normalized symmetrical GLCM, N is the number of gray levels in the image. The normalized symmetrical GLCM is created by first making the GLCM symmetrical and then normalized the GLCM by dividing each element by the sum of all elements. Notice that the weighting factor $(1 + |i - j|)$ emphasize the pixels pairs with close gray-scale values. This results in higher values for homogenous images.

Correlation is a measurement of how correlated a pixel is to its neighbor over the whole image; that is:

$$\text{Correlation} = \sum_{i,j=0}^{N-1} P_{ij} \frac{(i-\mu_i)(j-\mu_j)}{\sigma_i \sigma_j}$$

σ^2 is the variance of the intensity of all reference pixels in relation to the GLCM, calculated as $\sigma^2 = \sum_{i,j=0}^{N-1} P_{ij}(i - \mu)^2$. High correlations values indicate high local grey level dependency (Lubner, 2017).

CHAPTER 3

THE USE OF PHANTOMS FOR EVALUATING CT SYSTEMS

3.1 Introduction to Imaging Phantoms and Three-dimensional Printing

An imaging phantom is an object with specially designed features that serve as surrogates for human anatomy when investigating the performance of various imaging modalities. They are widely used in the medical imaging field as the gold standard for calibration and registration to ensure the reliable and quantitative quality assurance of the noise, resolution, and contrast in the imaging system. Though they are sufficient for delivering standard quality assurance for the imaging systems, the current phantom are often still rudimentary in their shapes, material compositions, and complexity. With traditional molding manufacturing techniques, complex geometries and fine anatomical textures of the human body are difficult to replicate. In addition, the high cost of the phantoms is a disincentive for any customizations and modifications to the standard practices that lead to more accurate and precise performance assessment of the imaging system. 3D-printing technology can overcome these constraints and make performance assessment more task-driven, versatile, accessible and accurate. Firstly, 3D printing technology is able to render more complex structures by using, for example, images extracted from an imaging scanner or through the use of procedurally generated textures. Secondly, 3D printing is helpful for developing patient-specific phantom because of the relatively low small batch production cost. Finally, 3D printing provides more flexibility in the phantom production process, allowing us to directly print the phantoms or indirectly produce a mold of the phantoms that can be injected with other tissue equivalent materials (Filippou, 2018).

3.2 Traditional Imaging Phantoms

Currently, the most popular commercial phantoms that are used in clinical practice include image quality phantoms and anthropomorphic phantoms. Image quality phantoms are often comprised of several different layers, each of which is designed for evaluating specific criteria of the image quality. The purpose of the phantom is to provide an overall evaluation of the performance of the imaging system, and to find protocols that can achieve better image quality while minimizing radiation dose. An example of an image quality phantom is the CBCT electron density & image quality phantom (figure 7), which comprises of five layers. The CT number linearity and slice thickness layer (figure 7A) includes six cylindrical chambers that enclose six rods made of air, low density polyethylene (LDPE), polystyrene, acrylic, Delrin and Teflon for measuring the contrast to noise ratio and the HU accuracy. There are three angled air channels forming an equilateral triangle at the center of this slab. They are used to measure the slice thickness sensitivity of the imaging system. The uniformity layer (figure 7B), made consistently with the same epoxy resin, is used to measure the ability of the imaging system to produce uniform images across all directions and if there are image artifacts. Constituting three sets of low contrast rods with linear attenuation differences of 0.5%, 1%, and 2% relative to the background material, the low contrast layer (figure 7C) measures the system's ability to detect low contrast difference. Each set contains seven different cylindrical rods with different diameters, where the cross section and volume ratio between two adjacent rods is 0.5. Spatial resolution layer (figure 7D) has 16 different line pairs starting with 1 lp/cm as the lowest spatial frequency and 1 lp/cm increment between the adjacent rods. The line pair patterns are 12mm in height in the longitudinal axis and can be used to evaluate the MTF and PSF of the imaging

system. The electron density phantom (figure 7E) is a customizable slab that simulates the abdomen (oval shape) or the head (circular shape). Eight plugs with different tissue equivalent attenuation coefficients could be placed at any of the 17 cylindrical cavities at different locations for user to evaluate the measurement offset from the central axis. This slice of phantom allows the technologist to devise the optimized diagnostic scanning protocol for real patients (CIRS, 2013).

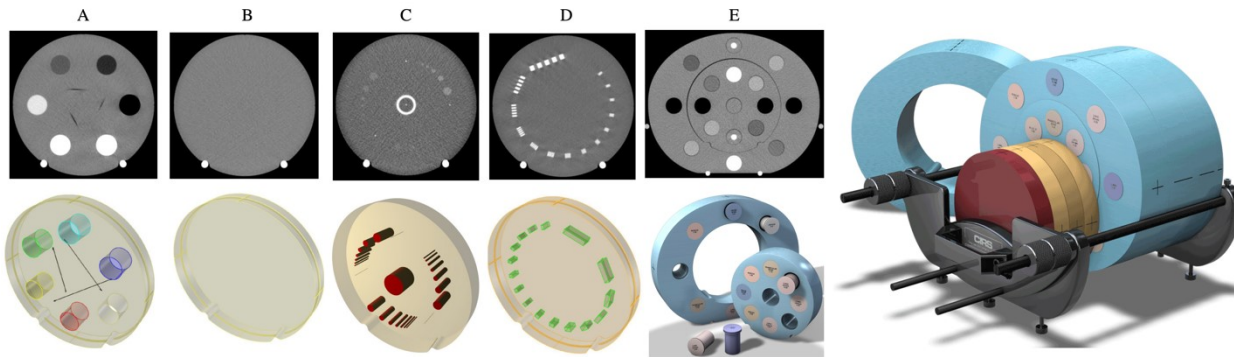


Figure 7. Image Assessment Phantom. A – CT number linearity and slice thickness layer; B – uniformity layer; C – low contrast layer; D - spatial resolution layer; E- Electron density phantom (CIRS, 2013).

Unlike the image quality phantoms that are designed for evaluating specific image quality criteria and thus have a more structured and organized configuration, anthropomorphic phantoms have more complicated structure and geometry that resemble the shape and size of human anatomy. The goal of these phantoms is to produce CT image or volumes that look similar to the actual clinical images. One example anthropomorphic phantom is the multipurpose chest phantom (figure 7). This phantom, $43 \times 40 \times 48$ cm in size and 18kg in weight, represents a male chest torso. The frame of the phantom includes the ribs, sternum, clavicles, spinal cord, and scapulae. Inside the main frame there are three main detachable inner compartments that

represent the tracheobronchial tree, the heart, and the abdomen (including the diaphragm). Including in the phantom are 15 simulated tumors with 5 different sizes (3, 5, 8, 10, 12mm) and 3 different sets of HU (-800, -630, 100). (Kyoto Kagaku CO. LTD, 2019)

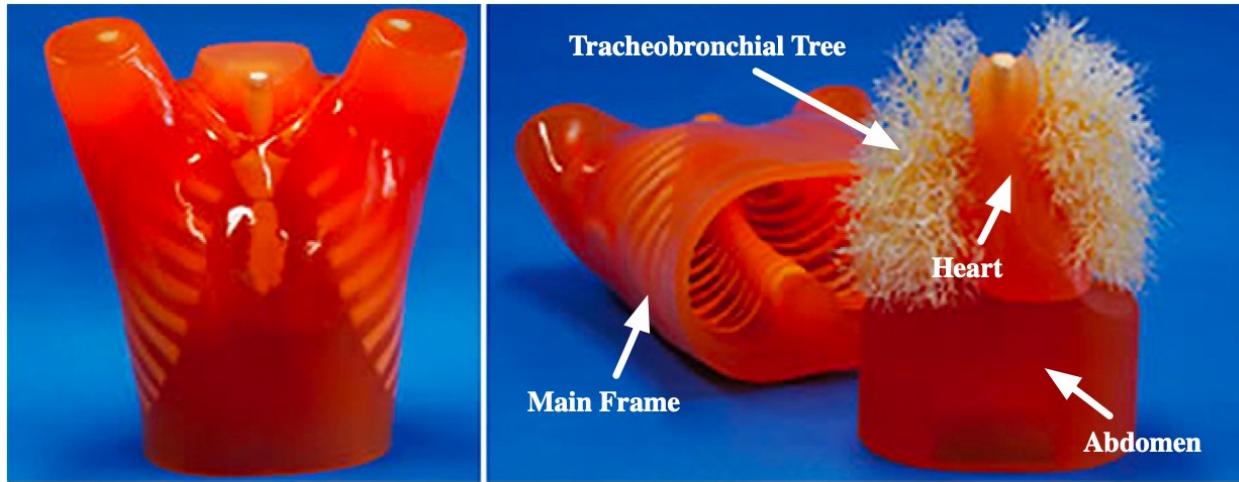


Figure 8. Multipurpose Chest Phantom Kyoto Kagaku N1 "LUNGMAN" (Murata et.al., 2019)

3.3 Introduction of Rapid Prototyping and Manufacturing

Rapid prototyping and manufacturing (RP&M) methods have gained significance and rapidly spread in the realm of aerospace, automotive, component, and medical applications. Initially, the company that pioneered this technology 3D systems coined this technology as Stereolithography, or 3D printing. Nowadays rapid prototyping is not confined to 3D printing, but as an umbrella term that refers to the process of producing a three-dimensional object that carries high level resemblance of the design intent.

The popularity of RP&M is well-deserved in its own right. Enhanced visualization capacity provides the first-tier benefit that bridges the gap between the different stakeholders (engineers, designers, technicians, and managers) for better communications, analysis and further

development in the means of an actual full-size model. Instead of two-dimensional drawing, developers can now discuss their ideas with scaled plastic prototypes with complex structures exacting the intended features. This kind of advantage is substantial because the actual object can be very different from reading the blueprints or computer aided design (CAD) images of a complex object. Interpretation of the actual object and the blueprint could be very different, and the ability to have a first-hand interaction with the actual object can help the developer identify the errors. The reduction of error significantly reduces product cycle time and cost compared to the conventional models.

Verification is one important step in the design control to attest that the design output matches the requirement of the design input. RP&M can resolve this dilemma by quickly generating the prototype to verify that the design contains the desired feature and inspecting errors or design mismatches with user needs early in the design cycle. This ability empowers decision making and increase the product quality. Verification of physical characteristics such as strength, operational temperature limits, fatigue, corrosion resistance, etc., also doesn't need to wait for a fully developed prototype but can start tinker with the design and add/remove features.

Additionally, RP&M provides a practical method for improving the quality of product through optimization. Optimization could be very expensive and time-consuming using the traditional manufacturing methods, but with RP&M the design teams can iterate and build multiple design prototypes and select the optimal design. (Jacobs, 1993).

In this work, we combine the advantages of RP&M design and production with validation phantom investigation for application to CT system technology, and protocol design and optimization.

3.4 A Modular Liver Anthropomorphic Phantom

The above anthropomorphic phantom allows for lung-specific customization. Lung nodules can be inserted inside the cavity of the anthropomorphic phantom. However, the abdomen interior part of the anthropomorphic is a solid and does not allow specifically designed inserts to be plugged in. To enable the testing of CT system performance for liver-specific CT protocols, we replicated the abdomen phantom with traditional silicon room temperature vulcanizing molding and resin casting. Three steps are involved in fabricating the replica of the abdomen phantom: (1). Creating the Molding Framework; (2). Creating the Silicone RTV Mold; (3). Resin Casting of the Abdomen Phantom. The materials that are used in the replication process includes 5 pieces of foamboards, Prosil 1025 RTV Silicone Rubber Mold Kit, and Castin'Craft Clear Polyester Casting Resin Kit.



Figure 9. Essential materials used to cast the anthropomorphic phantom. A – Foamboard; B - Prosil Silicone RTV Mold: left - silicone rubber; right - hardener C - Castin' Craft Clear Polyester Casting Resin: left - resin; right – catalyst.

3.4.1 Creating the Molding Framework

The replication of the abdomen phantom started with creating a structure as the container for the liquid silicone mold to transcribe the detailed surface features of the abdomen. The design of the frame should also consider minimizing the silicon mold materials. We used the foamboards to create such a framework. Placing the abdomen phantom above the foamboard, we delineated the outline of the maximum slice area (the bottom area). We created four layers of such frames by repeatedly cutting out the contour of the bottom slice for four times. Stacking one complete foam board and the four hollowed layers with hot glue, we created the rudimentary framework. We cut off some smaller foam pieces to fill in gaps between some of the crevices and wrapped around the outer surface with plastic and paper tapes to avoid leakage. To bolster the placement of the abdomen phantom and create the space for injecting the silicone room temperature vulcanizing mold, we also created some thick rectangular silicone parts to place in the bottom and the surrounding walls of the framework to create gaps.

3.4.2 Silicon Room Temperature Vulcanizing (RTV) Molding

Room temperature vulcanizing (RTV) rubber silicone is an accurate and cost-effective rapid prototyping technique that allows replicating the surface and details of an original part by creating the frame around which an object is constructed. In this work, we use Prosil 1025 Silicone Rubber manufactured by Fiberlay Inc., Sarasota, FL. This product contains two-component materials, where Part A is the silicone base and Part B is the curing agent. As the name RTV suggests, the mixture of the two agents with a ratio of 10A:1B can be cured at room temperature by a condensation reaction. The surface of the original abdomen phantom was

sprayed with CRC general purpose silicone mold release to prevent the phantom from adhering too tightly on the finished mold. The abdomen phantom is then placed stably inside the foamboard frame. We measured the two parts of the Prosil with the volume 10A: 1B ratio in a bucket and mixed them thoroughly, and then poured the mixture into the slit between the original abdomen phantom and the framework until the abdomen phantom was completely covered inside the liquid mixture. We then waited 24 hours until the liquid hardened into silicone rubber mold.



Figure 10. RTV molding process. Left: the mold immediately after being poured into the frames. Right: the final product

3.4.3 Resin Casting of the Abdomen Phantom

Resin casting refers to the manufacturing process where the resin is hardened inside a mold to form specific shape. In our work, we use the Castin' Craft Clear Polyester Casting Resin. For every volume ounce of the resin we added $\frac{1}{3}$ drop of catalyst. The mixture of resin and the catalyst were well-mixed and were poured into the silicone mold. The resin and the frame were then transferred inside an airtight chamber at 120 °F for 6 hours and at room temperature for the resin be solidified for 72 hours (all at standard atmospheric pressure). The concrete resin was then removed from the mold. The abdomen phantom is replicated at this step. The abdomen phantom was manually drilled using an upright mill and boring tool to form compartments for four cylinders with 37.75mm in diameter and 40mm in height.

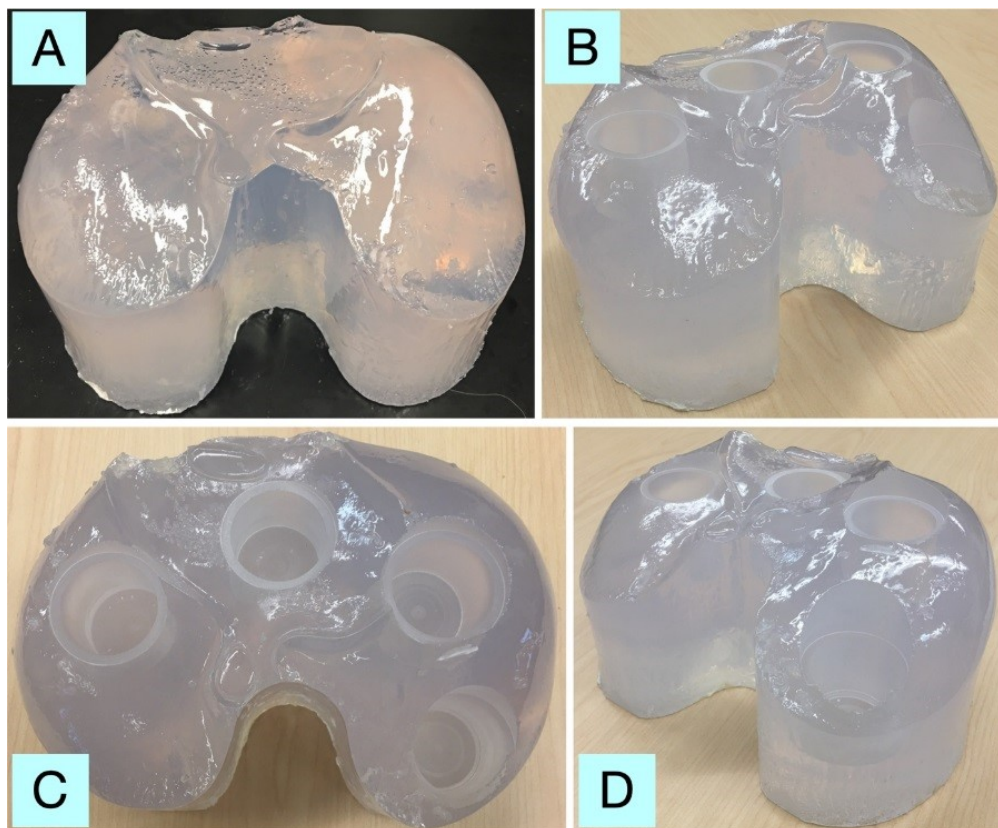


Figure 11. Abdomen Cast. A – replicated abdomen phantom. B-D drilled phantom by Milling; B- left view; C- top-down view; D-perspective view

3.5 Fabrication of Quantifiable Texture Phantom Inserts

Despite clinical significance of texture in classifying disease, there is no established method in examining texture with existing phantoms. Existing phantoms largely lack the sophistication presented by real-life scenarios (e.g. patient size, variability, organ texture, etc.) to provide a good quantification to characterize a CT system's ability to render texture. Though it is possible to 3D print an object derived from a CT image, clinically derived image volume will present noise and textures without ground truth, making it difficult to establish a realistic baseline for quantitative image analysis. Creating quantifiable texture that resembles the variable characteristics of the tissue texture is fundamental in establishing texture as the new image quality assessment methodology. To this end, we seek to create a method to produce high-resolution, reproducible, and standardized texture that allows us to evaluate the CT system capacity to render texture.

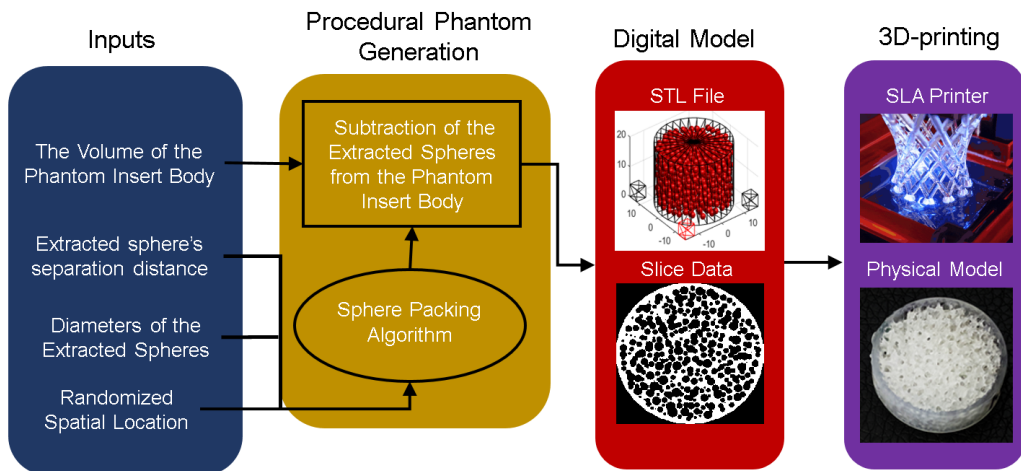


Figure 12. Overall Process for Creating Texture Phantom.

3.5.1 Generating Spheres

To create such a workflow, we generated a CAD model by randomizing the center locations of a large number of spherical voids inside a cylindrical volume. Thus, the texture phantom is the subtraction of many spheres from a cylindrical body. The first step to generate such a model is to generate the surface mesh of these spheres. The surface mesh of a single sphere can be represented by Standard Tessellation Language (STL) file, which is a face-set data structure that contains every surface vertex spatial coordinate. Since varying the diameter of the extracted sphere changes the porosity of the CAD model, we use the diameter of the sphere as the quantifiable feature in the phantom. With three different realizations in each set, we generated six sets of such CAD models with uniform spherical diameter evenly spaced between 1mm to 2mm. In addition to these phantoms with homogeneous spherical voids, we generated five realizations of the phantoms with heterogeneous (nonuniform) spherical voids where the diameters range from 1mm to 2mm. In this work, the cylindrical volume is 25mm in diameter, 8mm in height, and 0.5mm in outer wall thickness; Moreover, there is a user-defined amount of overlap between the spheres. These overlaps ensure that the spheres are interconnected so that ethanol could be channeled into the interior of the texture phantom to clean out residual resin (as part of SLA processing). By setting up the size of the spheres and the volume boundary conditions in which spheres can appear, we may procedurally generate the face-set data of the spheres that satisfy these defined conditions.

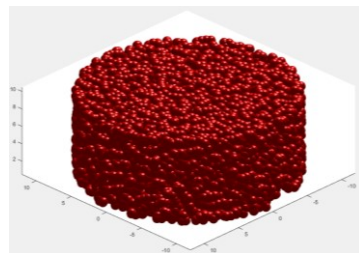


Figure 13. Example of the conglomeration of spheres within the confined cylindrical volume.

3.5.2 Compiling the Spheres and the Texture Phantom Body

With the available STL files of the spheres, we start to compile these spheres in OpenCAD. OpenCAD, a free software that have the capability to compile different shape together, can produce the STL file for the texture phantoms, as illustrated by figure 13. We imported the STL files of the spheres and subtract the spheres from the cylindrical body. We first clicked on “Preview”, which provides an overall rudimentary idea of the phantom’s appearance. Then, we click on “Render”. This process takes much longer (overnight) to generate. When this step is done, we can save the STL file by clicking on “Export as STL” to save the texture phantom.

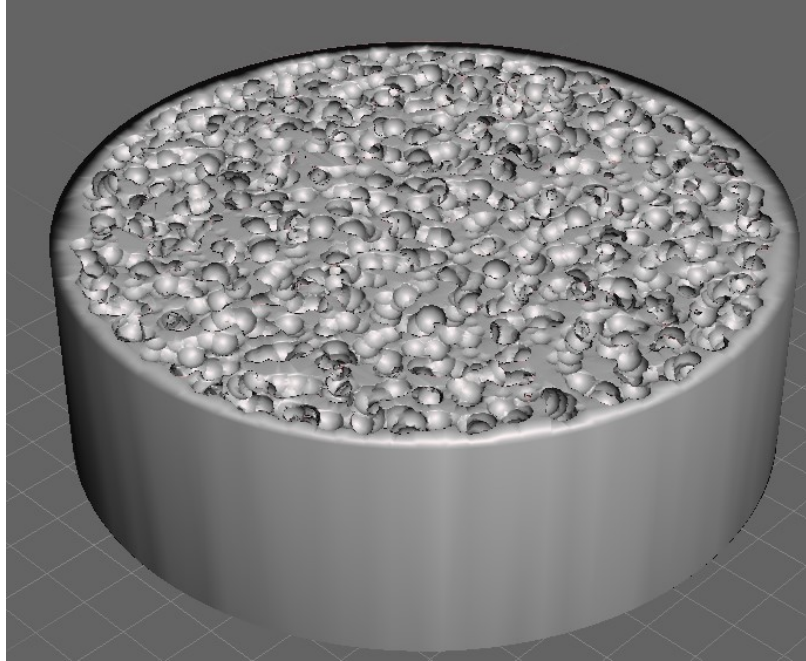


Figure 14. The Texture Phantom

3.5.3 Generating Print Support

For successful phantom printing, careful attention to print orientation and support material is required (e.g. thicker layers in the first couple print layers). Specially, in the meshmixer software package (Autodesk, San Rafael, CA), we first rotated the texture phantom at the upright position and then generated the support manually. In the Meshmixer under the tab Edit, we clicked on “Transform” and then inputted 90 in “Rotate X”. This will change the angle of the phantoms and position it at the right angle. Next, we elevated the phantom to be above the print plate. We inputted 20 mm in the tab “Translate Y”. The phantom was positioned at the right angle and level. To manually generate the support, we toggled the tab “Analysis” and clicked on Overhangs. We switched the Preset to “SLA/DLP Printer” and then dragged on the base of the phantoms to create the support. The goal here was to create the support as dense and vertical as possible for the support to be printed out. Inside of generating the support automatically, we generated the support by click and drag. This is because the tip of the automatically generated support could adhere to the inner compartment of the texture and tainted the texture.

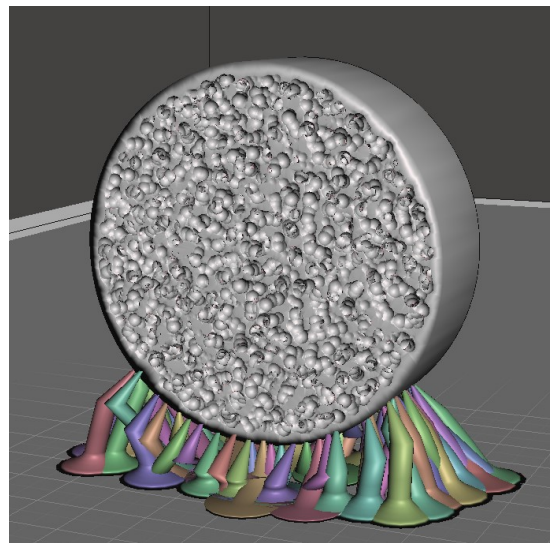


Figure 15. The Texture Phantom with Support

3.5.4 Stereolithography Process

These CAD models were fabricated with Clear Nex resin in a high-resolution stereolithography (SLA) printer (Peopoly Moai, Hong Kong), as illustrated in figure 15. Since the printer is controlled through the “GCODE”, procedure language we need to convert the STL file into GCODE using the CURA software package. Opening the STL file in CURA, we dragged the texture phantoms at the back-right corner of the print plate. Below is a table for the print setting that we used in printing our texture phantoms:

Table 1. Setting for the CURA

Layer Height	0.05 mm
Initial Layer Height	0.1 mm
Wall Thickness	0.6 mm
Top/Bottom Thickness	0.2 mm
Infill Density	100 %
Print Speed	130 mm/s
Travel Speed	300 mm/s
Initial Layer Speed	4 mm/s
Number of Small Layer	5

After the GCODE had been created, we saved it in an SD card. This SD card can be inserted inside the SLA printer. Each phantom was printed individually, and we detached it out of the print plate immediately after the print had been completed and removed the support. The printed sample was purged with 97% isopropanol alcohol solution and was vigorously shook inside a container to maximally clear out any uncured resin inside the extracted spheres. The samples were later cured under UV light for 1-2 hours.

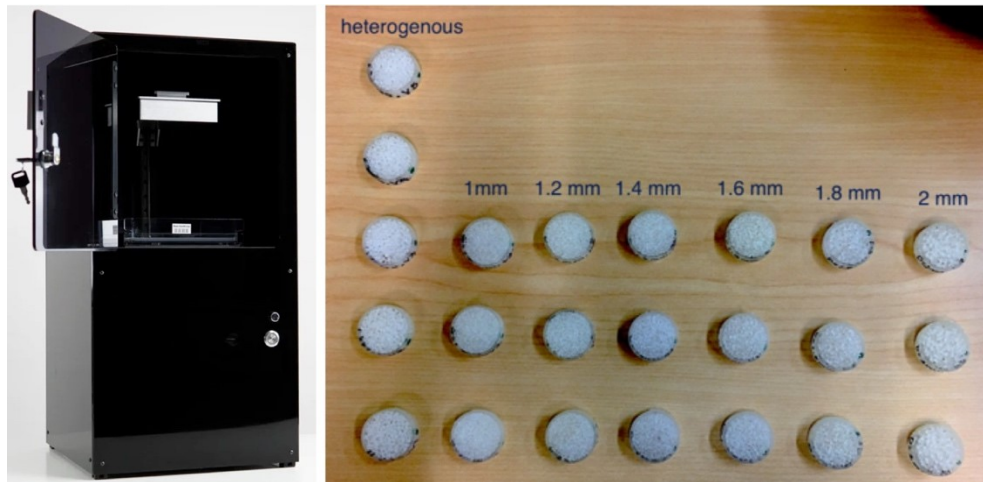


Figure 16. Printer and Print Objects. Left: Peopoly Moai SLA printer; Right: Printed Texture Phantoms.

3.6 Investigation of the Potassium Phosphate's Concentration vs. CT Contrast

As printed the phantom inserts have a CT contrast equal to the contrast between the cured resin and air. However, we would like the capability for arbitrary contrasts – e.g. through the introduction of a liquid to fill the voids with a known attenuation level. Here, we investigate the use of a potassium phosphate solution to achieve arbitrary contrast. We begin with an experiment to find the linear correlation between the potassium phosphate concentration and Hounsfield value. To this end, we made different concentrations and scanned them to measure the Hounsfield numbers. By finding the linear correlation, we may control the contrast for the CT images to simulate the realistic condition.

Seven vials with concentration(mg/ml) 0, 30.2, 29.12, 56.96, 65.89, 74.81, 200 were placed inside the vial holder and scanned for their respected Hounsfield values (figure 16). Each of the vial have been annotated separately with their hand-crafted labels for masking and measurement of the mean CT number. We scanned them with a custom conebeam CT bench with a Varex Paxscan 4343CB detector and Varex Rad-94 x-ray tube (Salt Lake City, UT) at 80 kVp, 40 ms, and 10 mA using 50 micron isotropic voxel with FBP reconstruction. The region of interest (ROI) was selected and the Hounsfield values are measured by averaging the trans-axial slices within the ROI. The linear correlation of the concentration (unit: mg/ml) and Hounsfield value was found to be:

$$HU = 2.418 c - 1.060$$

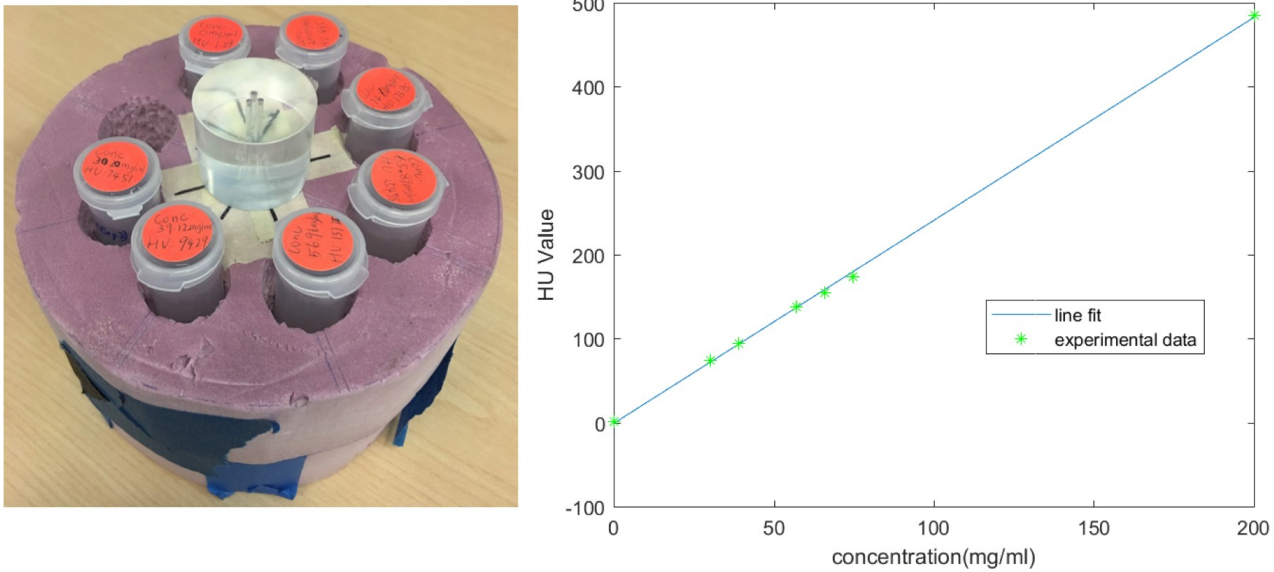


Figure 17. Correlation of Concentration and Hounsfield value. Left: Vials and its Holder; Right: the experimental data points(green astrisk) and the Linear Correlation Curve

With this equation, we can produce arbitrary contrast levels in the CT image by varying the concentration of the potassium phosphate solution. To maintain the consistency of the liquid presented in the CT image, we vacuumed to 25 inHg using AccuTemp-09s vacuum system (Across International, Livingston, NJ) and let the liquids stay overnight to remove the air bubbles.

3.7 Combining Elements into a Modular Texture Insert

Up until this point, we have described the complete methodology of fabricating the anthropomorphic phantom, the texture phantoms, and the formula for making the contrast-specific background. To generate the data, we need to combine all of these different parts together for the analysis. We collected data for the texture phantoms without any contrast-enhancement and texture phantom under realistic conditions. To collect the data for the texture

phantom without contrast enhancement, we either scan the texture phantom individually in the air or line up the different texture phantoms together to produce a scan that contains all the data (figure 17).

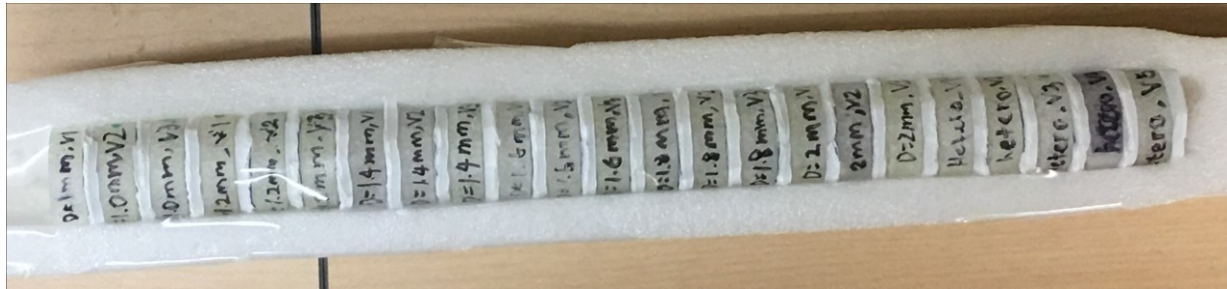


Figure 18. Lining Up the Texture Phantoms together with spacing between each other

We use potassium phosphate to emulate the contrast of iodine-enhanced hepatocellular carcinoma lesions. We immersed the texture phantom in potassium phosphate of 80 HU to create the simulated clinical scenarios (figure 18).

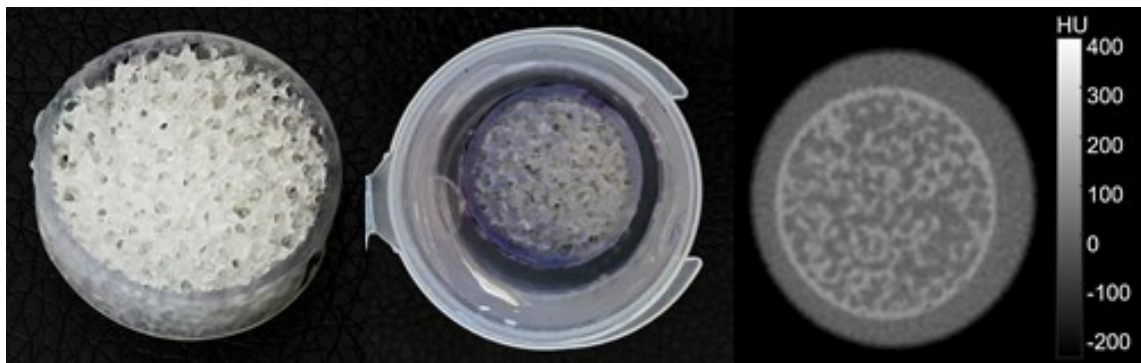


Figure 19. Contrast enhanced Texture Phantom. A) Sample SLA textured print. B) Print in potassium phosphate solution. C) CT scan showing a designed texture contrast of ~80 HU

To generate the realistic condition of scanning a patient, we placed the contrast enhanced texture inserts inside the abdomen cast, which could then go into the Kyoto Kagaku Lungman

phantom. The large and torso-shaped anthropomorphic phantom simulates the non-uniform attenuation of human anatomy and permit evaluation of texture with the added noise properties and scatter patterns from the real patients (figure 19).

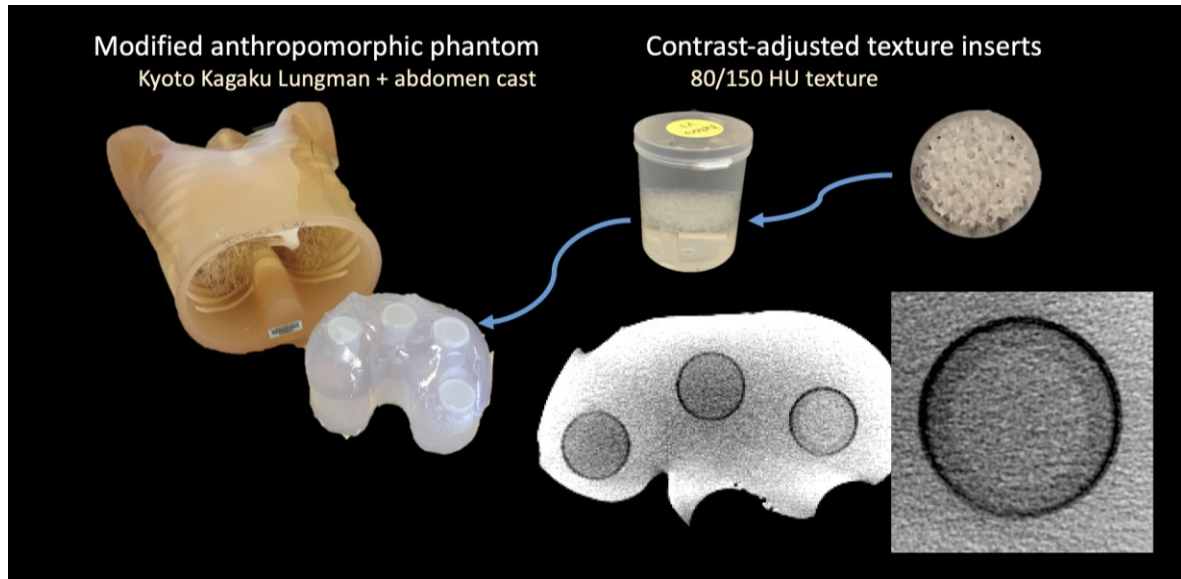


Figure 20. Texture Performance Assessment under Realistic Condition.

CHAPTER 4

PERFORMANCE ASSESSMENT OF TEXTURE REPRODUCTION

With the available quantitative texture phantoms, we want to develop a texture performance assessment methodology to evaluate the different CT systems. We compare the reproduction of textures on various systems including 1) a micro-CT, 2) a flat-panel-based cone-beam CT (CBCT) system, and 3) a commercial diagnostic CT scanner with high-resolution capability. Radiomic measures based on gray level co-occurrence matrices are investigated at a range of offset distances, and the capacities to reproduce the designed and scanned features across different imaging devices are compared.

4.1. Method

4.1.1. Phantom Scanning

Texture Phantoms were scanned in three different CT systems including 1) a Bruker SkyScan 1172 microCT (Billerica, MA) at 50 kVp and 200 μ A using 28 μ m isotropic voxels; 2) a custom CBCT system using a Varex Paxscan 4343CB detector and Varex Rad-94 x-ray tube (Salt Lake City, UT) at 100 kVp and 10 mA using 100 μ m isotropic voxels; and 3) a Canon Aquilion Precision CT (Otawara, Japan) at 120 kVp and 100 mA using two different protocols. Both a “normal” resolution (NR) and high resolution (HR) protocol were used on the clinical helical scanner. The NR protocol used a 100 m voxel size (in-plane) and 0.5 mm slice thickness

with a FC11 reconstruction filter and the HR protocol used a 50 m voxel size (in-plane) and 0.25 mm slice thickness with a FC15 reconstruction filter.

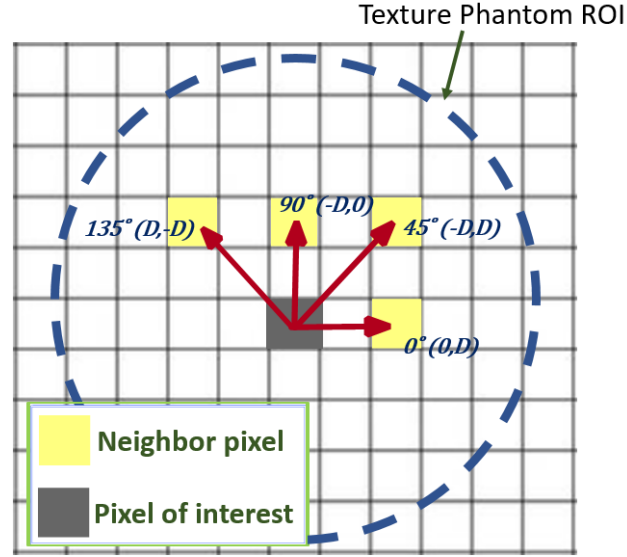


Figure 21. Illustration of the Four GLCM Offset Directions Used. Offset distance is computed as the distance to the origin in millimeters

4.1.2. Computation of Radiomics Features

To compare the ability of the 3D-printer and the various imaging devices to reproduce the originally designed textures radiomics features were computed. For computation of radiomics features, all scan volumes (e.g. microCT and HR-CT) were re-binned to a common $100 \mu\text{m}$ in-plane voxel size. Gray level co-occurrence matrices (GLCMs) were computed for a range of offsets from 0 to 3.0 mm in four principle directions (illustrated in Figure 20) using eight gray level bins. While many summary metrics of GLCMs can be computed, we focused on correlation and homogeneity. We compute an average GLCM-correlation and GLCM-homogeneity over the four directions, all trans-axial slices, and three (or five, for the heterogeneous inserts) realizations as a function of offset distance. Similarly, we compute standard deviation over the same ensemble.

4.2 RESULTS

Three sample texture inserts (homogeneous 1 and 2 mm, and heterogeneous 1-2 mm spherical voids) are shown in Figure 21. We note that there is a difference between the digital design and the 3D-printed result. This is evident from the micro-CT scans, which are serving as a surrogate truth image (based on the very high-resolution scan). In particular, we see that the SLA resin tends to cure “thicker” than the original digital design (in part due to the size of the laser focal spot). This makes the plastic walls of the texture thicker with smaller internal voids. There are also subtle differences in texture that may have to do with incomplete removal of uncured resin between printing and the secondary curing step. Cone-beam CT and CT scans show the reproduction of the insert texture for each modality and the different acquisition modes/reconstruction filters. The CBCT and HR-CT images look similar while the NR-CT images are clearly lower spatial resolution leading to a much different representation of the underlying textures. Additional differences between modalities are present due to positioning of the insert and the different slice thicknesses between modalities.

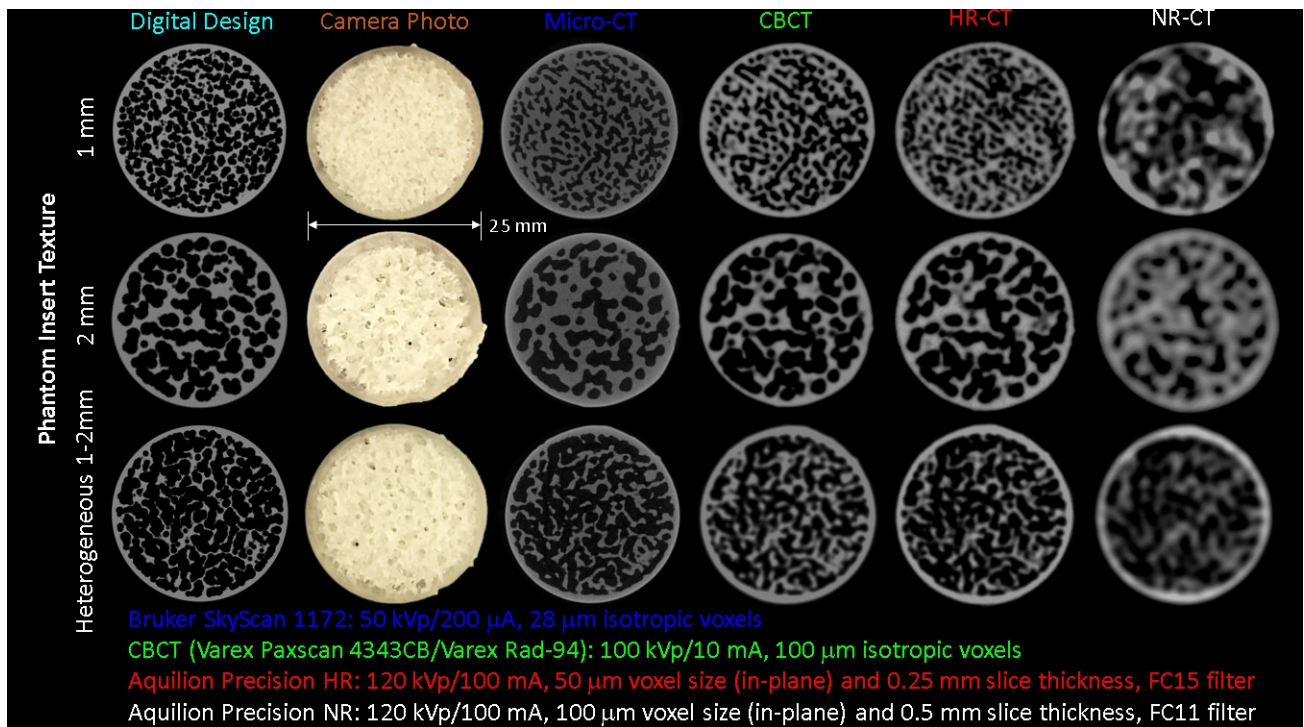


Figure 22. Qualitative Comparison of Texture Phantom Scans: three of the texture inserts with 1 mm and 2 mm homogeneous, and 1-2 mm heterogeneous spherical voids are presented. In addition to the digital design and a photograph of the 3D print, scans of one slice of the insert are shown for micro-CT, cone-beam CT, high-resolution CT (HR-CT), and normal resolution CT (NR-CT) are shown.

A summary of the radiomics measures investigation is shown in Figure 22. Both GLCM-Correlation (top row) and GLCM-Homogeneity are shown as a function of offset distance. A number of trends are apparent. GLCM-Correlation decreases from a value of one, tends to fall to a minimum at a value slightly smaller than the void/feature size, and then asymptotically approaches zero. The micro-CT ground truth suggests that we are able to reproduce the GLCM-Correlation of the original design and that printing differences do not affect this particular metric. In contrast, both CBCT and HR-CT do not reproduce this metric perfectly – instead extending the location of the minimum to larger values. This is likely due to spatial resolution loss. We note that CBCT and HR-CT perform similarly in this regard with the most significant differences at the smallest feature sizes. However, NR-CT shows increased discrepancy and loses a well-defined

minimum for the smaller feature sizes. Similar conclusions can be drawn from GLCM-Homogeneity; however, GLCM-Homogeneity and GLCM-Correlation refer to two different concepts.

The homogeneity analysis is very similar to the correlation analysis. Specifically, CBCT and HR-CT show very similar GLCM-Homogeneity across feature sizes suggesting a similar ability to reproduce texture, though different than the micro-CT ground truth. NR-CT is significantly different in its reproduction of texture and this is reflected in the GLCM-Homogeneity.

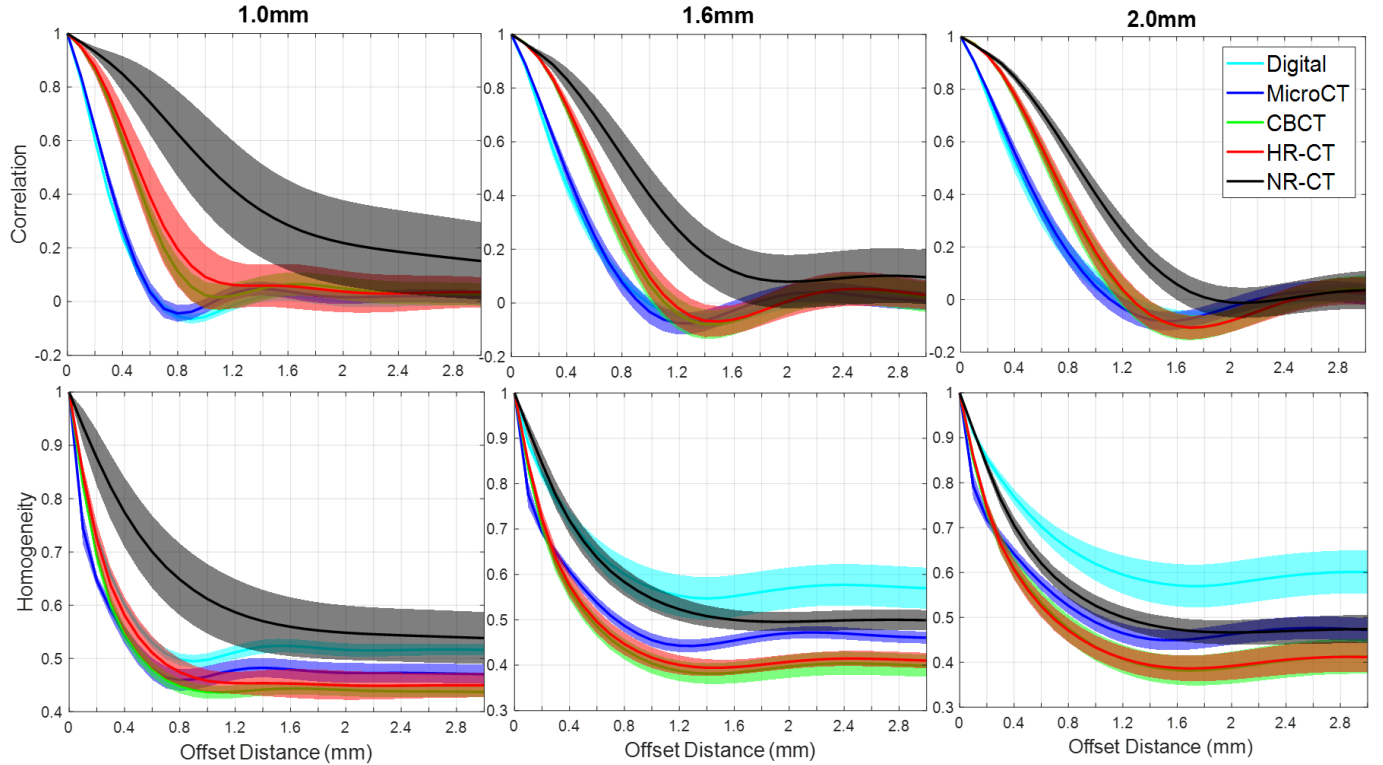


Figure 23. A Summary of GLCM Features. GLCM-Correlation (top row) and GLCM Homogeneity (bottom row), as a function of offset distance for the different homogeneous inserts (i.e. varying extracted spheres' feature size) and the different imaging modalities.

It is worth noting the apparent connection between the first minimum in the GLCM-Correlation and the intrinsic void/feature size in the designed textures. We plotted the GLCM-Correlation minimum as a function of feature size for each of the modalities and performed linear fits for all but the NR-CT data. These results are summarized in Figure 23. We see that there is a strong linear relationship between GLCM-Correlation minimum and feature size with strong correlation across imaging methods except for NR-CT which does not appear to capture this aspect of the texture very well and has no defined minima for the smaller feature sizes. Similarly, there is no distinct minimum for the HR-CT approach at the smallest 1.0 mm size. Thus, it is not straightforward to deduce intrinsic features size using GLCM-Correlation for NR-CT or for HR-CT at the smallest investigated feature size.

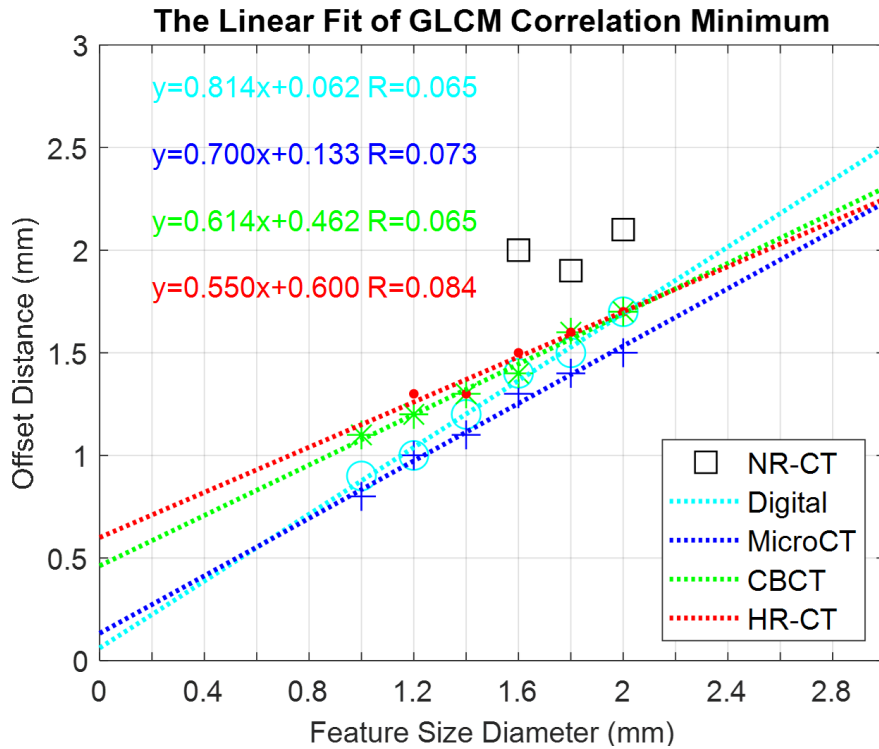


Figure 24. Plots of GLCM-Correlation Minimum for Different Modalities as a Function of Feature Size

Figure 24 shows the GLCM-Correlation and GLCM-Homogeneity for the heterogeneous inserts. These inserts have feature sizes covering the range of 1.0-2.0 mm. As such we see differences in the curves from previous studies – e.g., the GLCM-Correlation plots show a wider dip around the minimum due to the range of feature sizes. Similar conclusions can be drawn from this experiment as the prior homogeneous inserts. In particular, GLCM-Correlation is reproduced between the digital design and the micro-CT while GLCM-Homogeneity is not. Similar reproduction of radiomics between the CBCT and HR-CT methods is observed. NR-CT is significantly different in its radiomics, which can be attributed to the significantly decreased spatial resolution.

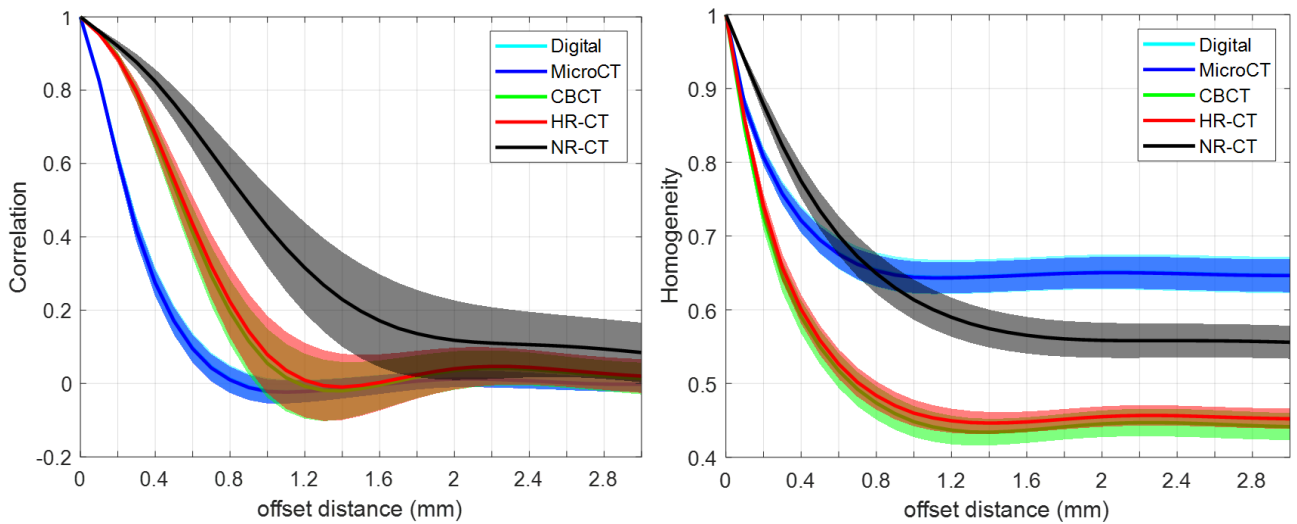


Figure 25. GLCM-Correlation and GLCM-Homogeneity for the heterogeneous inserts

When the plots of the contrast enhanced texture inserts in the anthropomorphic phantoms are included in the GLCM analysis, we found that the added noise and scatter properties of a realistic phantom are a significant factor in performance. Specifically, the GLCM correlation or homogeneity derived from these set of data do not produce the similar profile or curvatures

compared to the HR-CT or the NR-CT. This means that the noise produced from the anthropomorphic phantom overshadows the capacity of the scanner to capture the texture properties of the inserts.

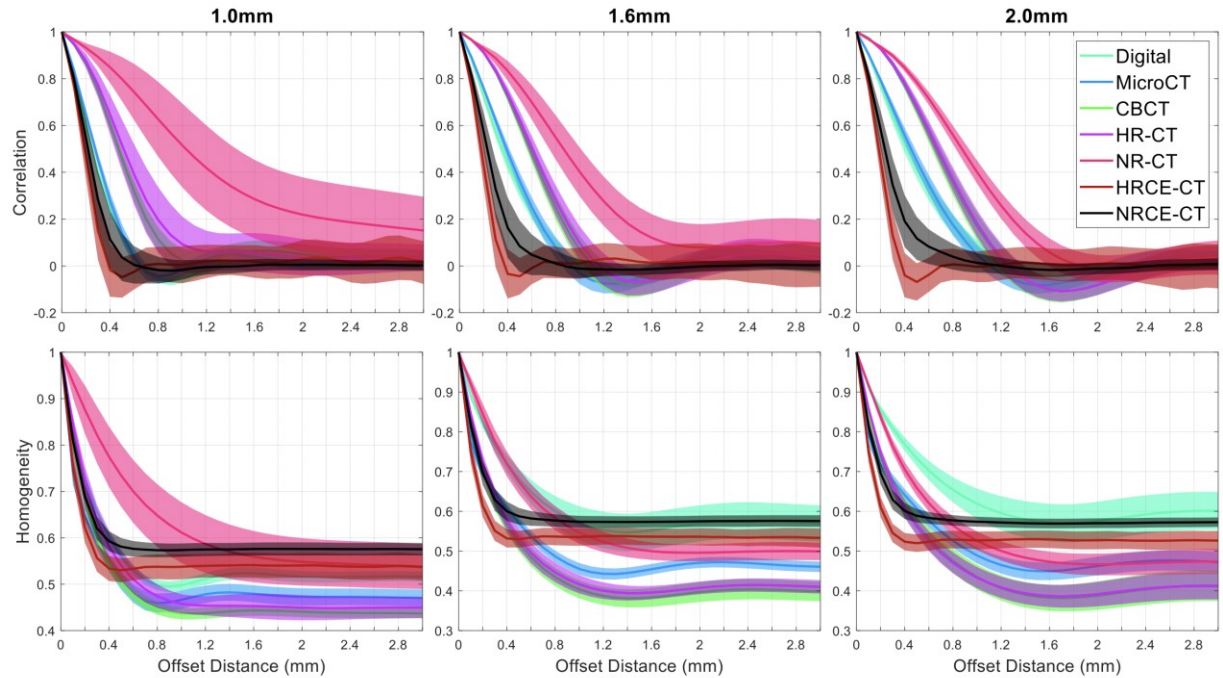


Figure 26. The GLCM Features with the Added Anthropomorphic Data Set. GLCM-Correlation (top row) and GLCM Homogeneity (bottom row), as a function of offset distance for the different homogeneous inserts (i.e. varying extracted spheres' feature size) and the different imaging modalities. HR-CT: High resolution CT; NR-CT: Normal resolution CT; HRCE-CT: High resolution contrast enhanced CT; NRCE-CT: Normal resolution contrast-enhanced CT; Only the contrast enhanced CT images are acquired inside the anthropomorphic phantom.

4.3 Discussion and Future Work

The radiomic analysis of the texture phantoms shows one way to analyze the CT system's capacity to render texture property. Without the anthropomorphic phantom. The HRCT shows more promising result than the NRCT. However, with the bulk property of the body, the clinical CT with the traditional iterative reconstruction doesn't replicate the behavior of the texture features measured by the microCT, but we hope to repeat the analysis again with the AiCE machine learning reconstruction to see if the improved reconstruction algorithm will perform better in texture reproduction.

In addition to the CAD-designed texture phantom, we also want to use liver sample (figure 26) to insert inside the anthropomorphic phantom to continue the radiomic analysis. This animal specimen provides a more realistic clinical representation because the sample includes not only the texture dispersity but also the vascular structures of the liver. By thoroughly studying the liver specimen, we can use the knowledge to help us design better liver lesion CAD model.

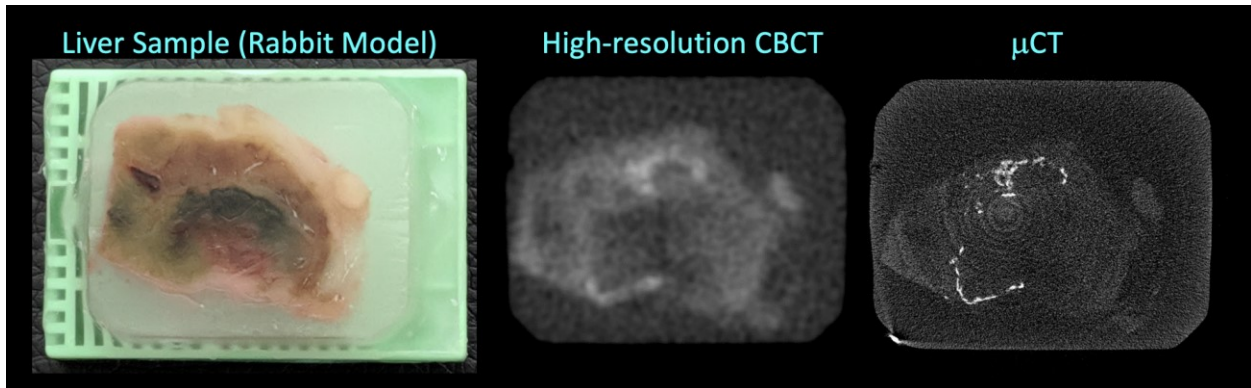


Figure 27. Liver Lesion with Iodine Enhancement from the Rabbit Model.

CHAPTER 5

OTHER 3D PRINTING MODULAR PARTS

5.1. Morphological Patterns

Texture is one of the most important features for identifying the tumor stages. Apart from the texture features that can be investigated with the 3D printed phantom, we also have developed other quantitative morphological models for analyzing other important indicators for physiological features. These morphological patterns include vascular stenosis phantoms, an annular phantom that models the sharpness of a lesion's boundary to the surrounding tissues, and a spiculated phantom that represents lesions with variable tissue's margins.

5.2 Design and 3D-print the Vascular Phantom

5.2.1 Vascular Stenotic Phantom Insert as the Performance Phantom

The primary goal of the vascular stenotic phantom is to investigate the limiting vessel size and contrast in arterial visualization. This is important, for example, in visualization of hepatic arterial chemoembolization. Hepatic arterial chemoembolization (HACE) is one way to treat patients with unresectable hepatocellular carcinoma (Pelletier, et. al.). HACE is intended to stop tumor growth while sparing the healthy liver tissue. Blood vessels are broadly spread in the liver. The majority of the blood that the normal liver cells received are supplied by the portal veins, while liver tumors are fed by blood supply from the artery. HACE takes advantage of this

discrepancy in the two cells and starve the tumor cells by injecting chemotherapy drugs into the hepatic artery to narrow and block the arterial blood supply.

One way to characterize the efficacy of HACE is through tracking the blockage of arterial vessels in the CT image. This high-resolution imaging task has similar obstacle to the texture imaging task where non-uniform attenuation properties of the body build up additional noise to the vascular characteristics. We design a CAD model that resembles the vascular stenosis in order to understand the capacity of the CT imaging system in rendering the vascular structures.

5.2.2 Design and 3D-print of the Vascular Phantom

The stenotic vascular phantom (figure 28D) is designed such that all 15 hollow cylinders are located radially throughout the cylindrical phantom body with 25mm diameter. For these hollow cylinders, there are five of the hollow cylinders with 4mm maximum diameter, four with 3mm maximum diameter, three with 2mm maximum diameter and one with 0.3 diameter (figure 28A). The outermost ring is composed of hollow cylinders with 4mm maximum diameter, followed by the medial ring of 3mm and 2mm maximum diameter and innermost ring of 1mm and 0.3mm maximum diameter. The hollow cylinders have three sections, where the diameters of the cylinders at both distal ends (10mm in axial direction) are uniformly distributed and the middle part of the cylinder tapered towards the middle (20mm in axial direction). The stenotic part of the cylinder is narrowest at the center in the axial direction, and linearly expand in diameter distally. The maximum and minimum of the stenotic phantoms can be found in table 2. It is important to note that the minimum diameter exists at the midline in the axial direction.

Table 2. Summary of the Range of Diameters of the Hollow Cylinders (Unit: mm)

Maximum Diameter	Minimum Diameter				
4	0.300	1.225	2.150	3.075	4.000
3	0.300	1.200	2.100	3.000	
2	0.300	1.150	2		
1	0.300	1			
0.3	0.300				

Figure 28 shows the schematics of the phantoms. From figure 28A, we can observe that the group with 4mm maximum diameter has counterclockwise orientation from widest to narrowest minimum diameter. Clustered on the same perimeter of the circle, the 2mm and 3mm maximum diameter groups are oriented differently from the widest to the narrowest minimum diameter, where 3mm group are on the left with counterclockwise orientation and 2mm group are on the right with clockwise orientation. This difference in the radial orientation helps us easily differentiate the two groups. On the very center located the 2mm and 1mm group. They are easy to spot based on the size of the diameter and the narrowing inner matters because the only one of the 2mm groups has a narrowing middle section. Figure 28C gives us an example of the modeling of the narrowing vessel. It is clear that the attenuation of the vessel is homogenous in both directions and turns to the narrowest in the midline in the axial direction. Figure 28D is a perspective view of the stenotic vascular phantom.

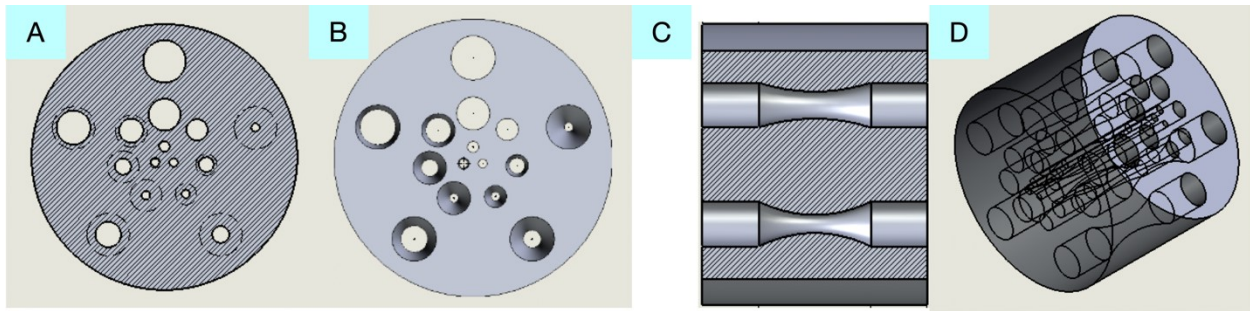


Figure 28. Schematic illustration of the stenotic phantom. A - top-down view of the sketch of the design. B - top-down view of the Solid Design. C - cross section view of the stenotic phantom. D - x-ray perspective view of the stenotic phantom.

After designing these phantoms, we use the Peopoly Moai printer to print the vascular phantom. Figure 29 is the 3D printed phantom. All the features are printed as expected. We cleaned the phantom with 97% isopropanol alcohol to fully clear out the liquid resin that might remain inside the tunnel. From visualizing the physical phantom and pouring alcohol through the tunnel, we observed that the tunnels are fully cleared, and narrowest part of the tunnel fully printed.

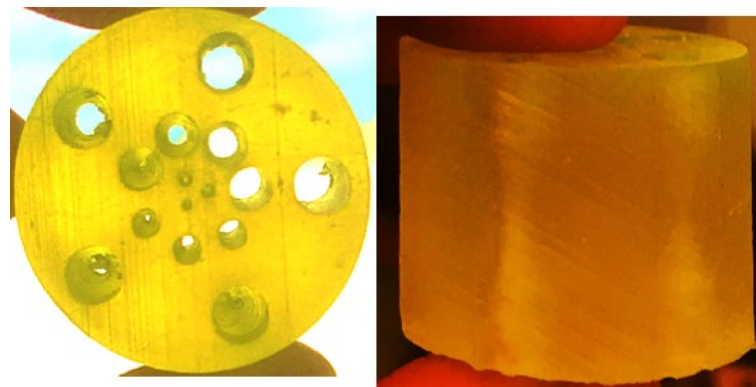


Figure 29. 3D Printing Stenotic Phantom

5.2.3 Vascular Phantom Result

Figure 30 shows the reconstructed CT image of the phantom. This is done with a custom CBCT system using a Varex Paxscan 4343CB detector and Varex Rad-94 x-ray tube (Salt Lake City, UT) at 100 kVp and 10 mA using 100 μm isotropic voxels. The CT reconstructed image verifies that the tunnels are cleared without resin residuals stuck in the tunnels. These features are illustrated clearly shown in the three cross-sectional views of the image. The narrowest parts of the tunnels are distinctly shown, indicating that the resin residual has been cleared in the physical model. Future studies will include visibility with infused contrast agent (e.g. iodine or potassium phosphate solution).

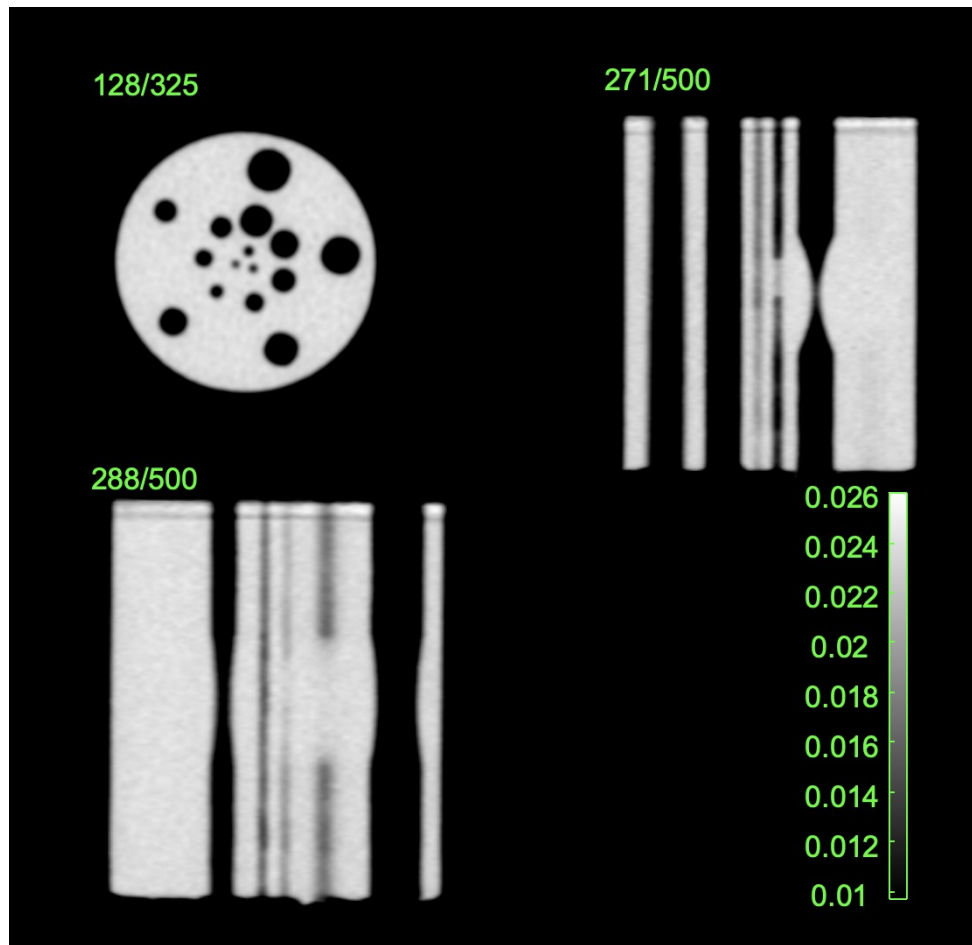


Figure 30. CT scan of the phantoms

5.3 Annular Phantoms

5.3.1 Clinical Implications

Nodules are commonly referred as the abnormal aggregation of cells in the body. They are reflected in the CT images and exhibit interesting features to be investigated as diagnostic hallmarks. The distinction between benign and malignant tumor has high practical value because it can prevent unnecessary surgical resection. One important diagnostic of a lesion is the sharpness of the margin. 3D-printing of such “soft” margins is difficult (especially at arbitrary contrasts). Thus, we adopt an approach where an annulus is printed, and the interior is filled with a liquid of particular contrast – in effect a “stepped” phantom with three contrast levels and variable step size to control how “soft” the edge is.

5.3.2 Computer-aided Design of the Annular Phantoms

The annular phantom is a tube-shape cylindrical structure with varying thicknesses. By varying the contrast level injected to the annular tubes, we are able to create different blurriness in the margin for the CT image. There are seven targets in total with 6mm outer diameter. The wall thickness of these seven phantoms vary uniformly from 0.1mm(A) to 0.7mm(G). Figure 31 shows the design schematics for the annular phantom. The different tubular structures go in clockwise direction and the tube with largest thickness is located in the center of the phantom.

Annuli Phantom Design Input (unit in millimeter)

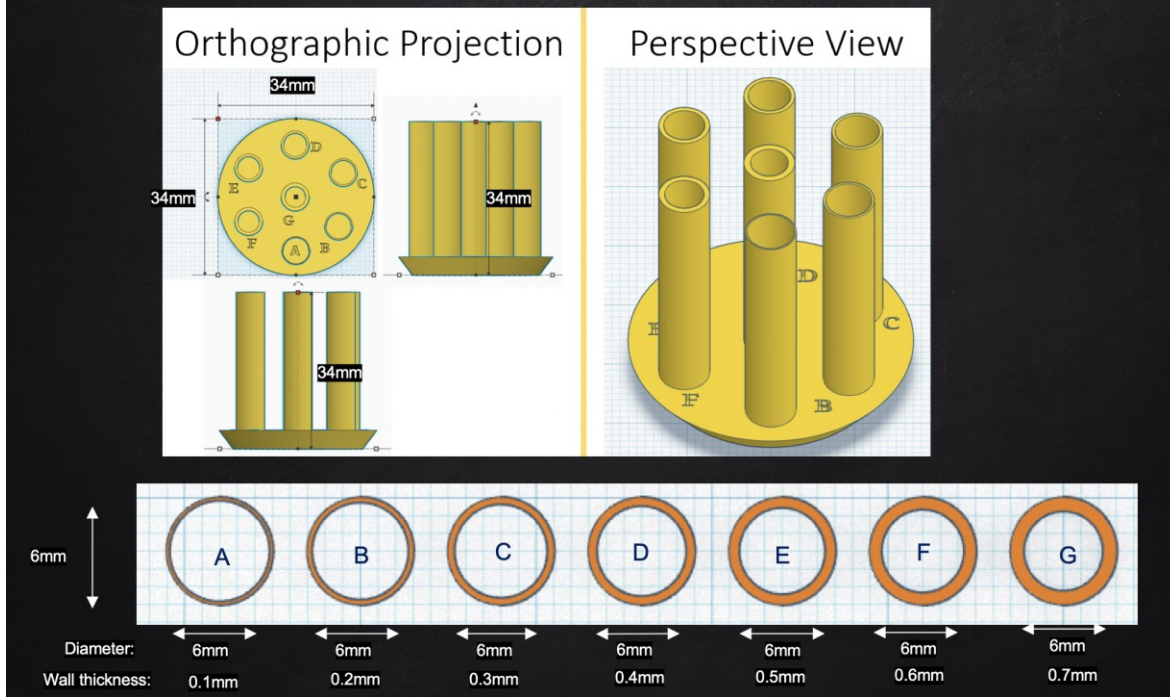


Figure 31. Schematics of the annular phantom design

5.3.3 CT Scans of the Annular Phantoms

The annular phantom can be placed in a plastic container, allowing a background contrast to be filled outside the tubular structure. The inner part of the tubular structure, which can also be filled, is going to be referred as the interior contrast. We designed four sets of experimentations with varying degrees of contrast levels. It is known that the contrast for the 3D printed resin is 150. For the first experiment, the background is filled with water, and the interior part is filled with potassium phosphate with concentration equivalent to 300 HU. The second experiment is designed such that the background contrast is 50 HU and the tube filling contrast is 250 HU. The third experiment has 100 HU in the background contrast and 200 HU in the interior. The last experiment has 125 HU in the background contrast and 175 HU in the interior.

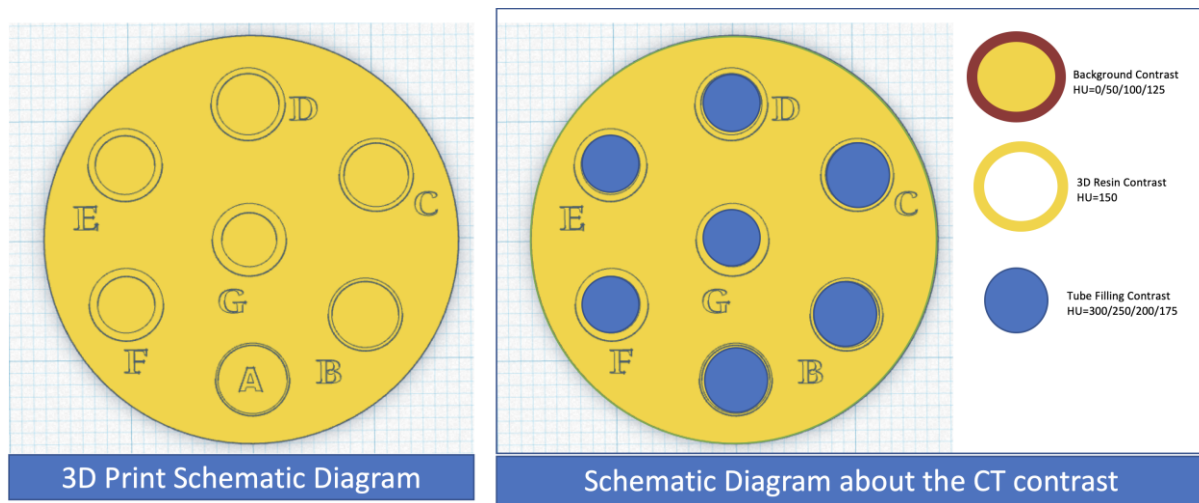


Figure 32. Schematics Diagram Showing how the Phantoms are Filled

The acquisition is done with a custom CBCT system using a Varex Paxscan 4343CB detector and Varex Rad-94 x-ray tube (Salt Lake City, UT) at 100 kVp and 10 mA with small focal spot. There are 360 frames in total and the exposure time per frame is 40ms. The reconstruction is done with filtered back projection using 100 μm isotropic voxels and the ramp filter's cutoff frequency is 0.8.

5.3.4 Estimating Edge Sharpness

To systematically assess edge sharpness, we adopted a model-based fitting approach. We designed a model specifically parameterized by $x_{center}, y_{center}, r, \mu_{phantom}, \mu_{background}$ for the targeted regions such that:

$$F = \sqrt{(X - x_{center})^2 + (Y - y_{center})^2} < r$$

$$F = F * (\mu_{phantom} - \mu_{background}) + \mu_{background}$$

where X and Y have the same size as the acquired CT image. x_{center} and y_{center} is the center of the spiculated lesion, and $\mu_{phantom}$ and $\mu_{background}$ are the attenuation coefficient for the modeled phantom(interior contrast) and the background. We convolved a gaussian filter with a circular mask modeling the uniform lesion with blurred edge. The Gaussian filter is

$$G = \frac{1}{\sqrt{2\pi\sigma^2}} e^{-\frac{(X_{filt}-\mu_x)^2+(Y_{filt}-\mu_y)^2}{2\sigma^2}}$$

where X_{filt} and Y_{filt} are half of the image size, and μ_x and μ_y are the midpoint of the horizontal width and vertical filter height, respectively.

After the convolution, we normalize by dividing the product of the convolution (H) by its maximum:

$$H = F \otimes G$$

$$H = \frac{H}{\max(\max(H))}$$

The objective function is

$$\mu = \text{argmin} \|H - \text{data}\|^2$$

We use fminsearch to estimate the model parameters $x_{center}, y_{center}, \mu_x, \mu_y, \sigma^2$

5.3.5 Results

The CT reconstructed images are shown in figure 34. For the 4 sets of phantoms with different contrast ratios that we designed, we have 4 different CT reconstructed images. Recall, the first set (A) has 0 HU in the background and 300 HU inside the interior. The second set (B) is 50 HU in the background and 250 HU in the interior. The third set (C) is 100 HU in the background and 200 HU in the interior. The last set (D) has 125 HU in the background and 175 HU inside the interior. For A-D, the upper part shows the axial slice of the reconstructed image and the lower part shows the specific stimuli. For the specific stimuli, there are two parts where the upper part shows the single slice of the stimuli and the lower part shows an average slice of the stimuli. Figure 34A shows the result where the contrast is the most conspicuous. The phantom with the thinnest wall of the 3D printed annular phantom does not show up in the image because the wall is so thin that fracture of the wall caused leakage. We can observe that there is an increasing blurriness in the boundary when the thickness of the wall increases. This observation holds true when the contrast ratio is equal to 50:150:250 or 100:150:200. However, when the contrast ratio is 125:150:175, it is hard to differentiate the margin anymore. This results from the smaller ascension gap of the Hounsfield unit values between the contrast agent and the 3D printed resin.

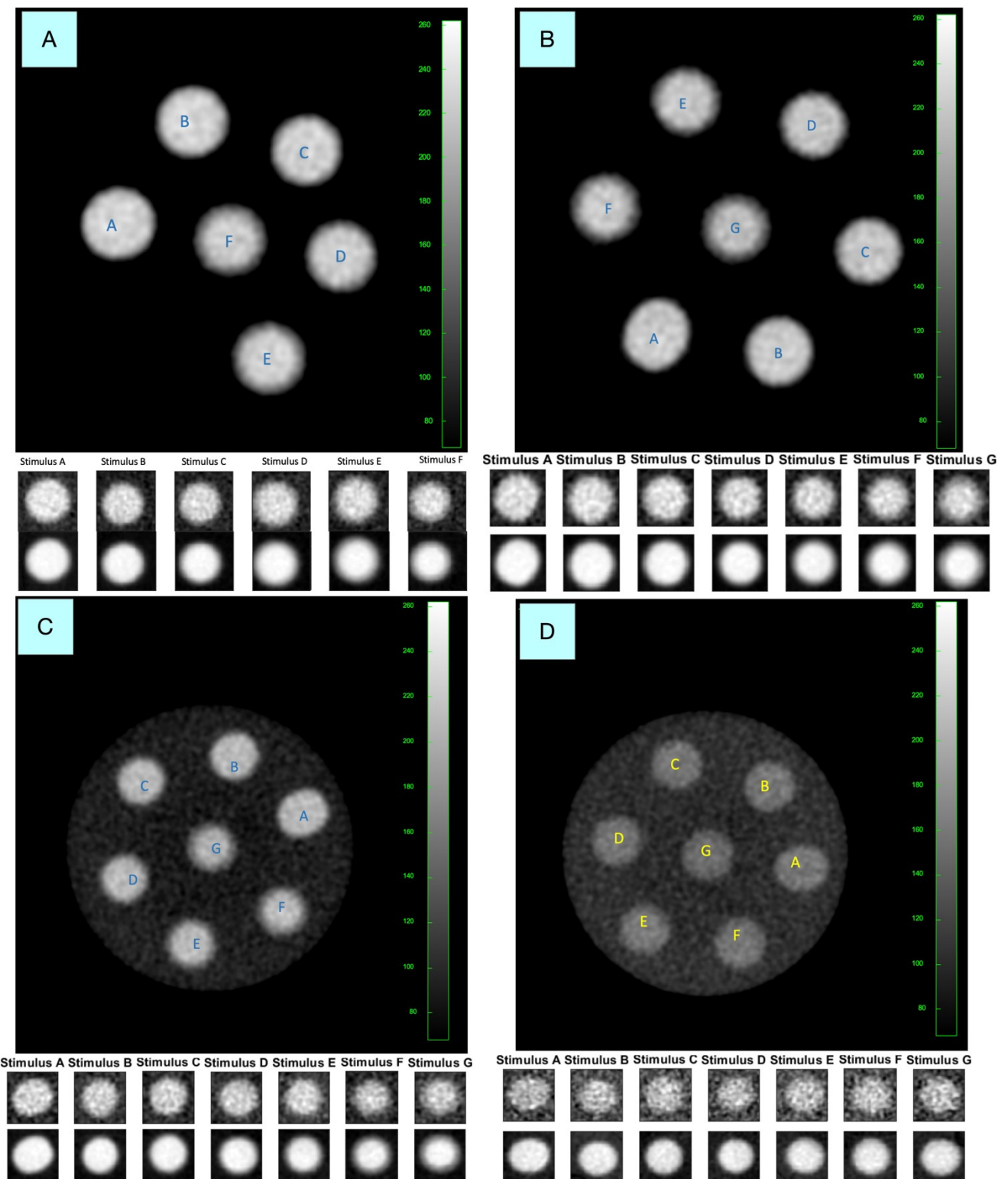
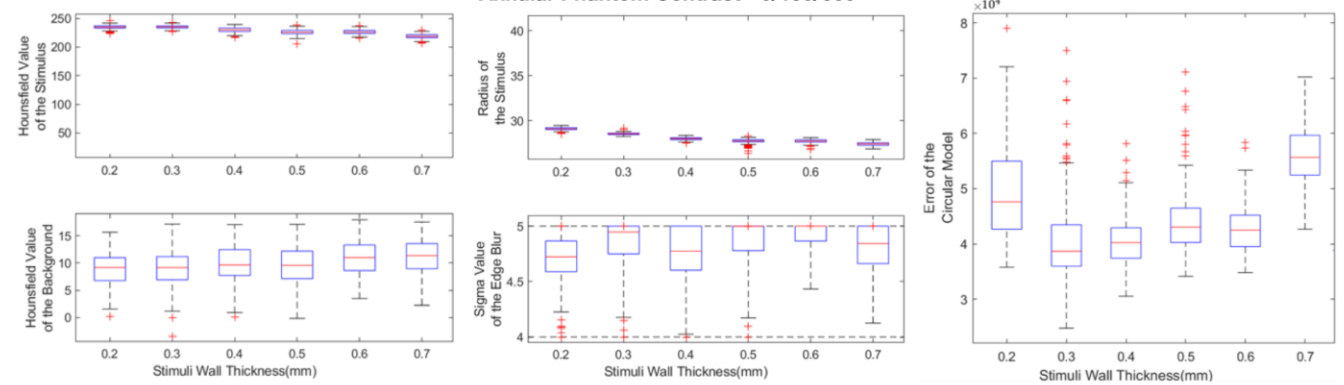


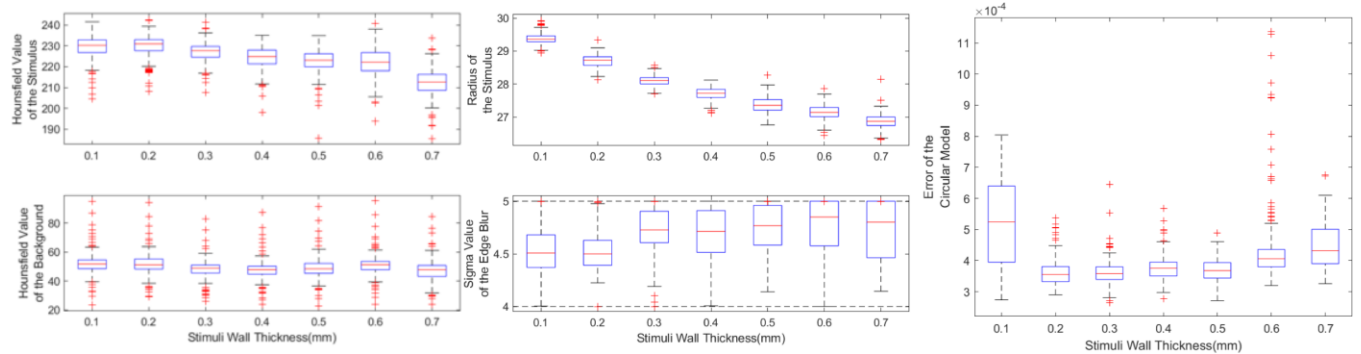
Figure 33. Annular Phantoms with contrast. A – Contrast ratio is designed as 0/150/300. B- Contrast ratio is designed as 50/150/250. C – Contrast ratio is designed as 100/150/200. D- Contrast ratio is designed as 125/150/175.

Figure 35 shows the results of the computational modeling of the image targets. When the designed contrast ratio is 0:150:300, the stimulus all stays at a stable range between 200 and 250 HU, and the background is ranged between 0 to 20 HU value. Although the actual stimulus Hounsfield value is lower than expected, it still presents a contrast difference with the tube walls. The background is close to zero, which shows a very distinct edge for the margin of the stimuli. When designed contrast ratio is 50:150:250, the stimuli show an average of 220 HU and the background shows an average of 50 HU. The stimuli's attenuation coefficient is lowest as the wall thickness is the largest. This is understandable because the margin of the stimulus is largely taken by the resin, which shows a lower Hounsfield value than the injected contrast agent. Therefore, the modeling takes an average of the circular regions that is much higher than the background value, where the resin and the injected contrast agents are all included in the modeling process. The same of effects also appears when contrast ratio is 100:150:200. For the first three sets of phantoms, there is a decreasing trend of the radius of the stimuli as the wall thickness increases. The Hounsfield value of the filling regions and the background also behave as expected. The error is within 10^{-4} and is uniformly distributed. We expect that the sigma value would show a linear trend related to the thickness of the annulus. This expected result needs to be investigated in future work.

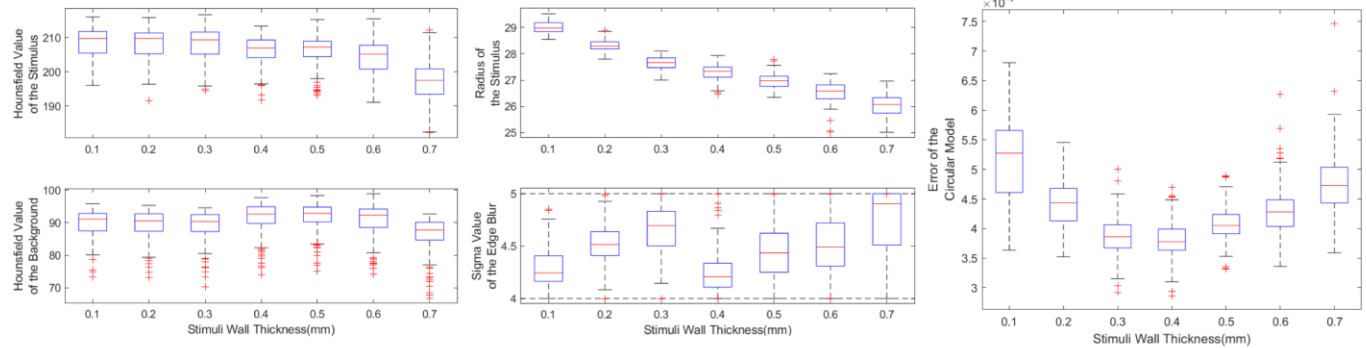
Annular Phantom Contrast - 0/150/300



Annular Phantom Contrast - 50/150/250



Annular Phantom Contrast - 100/150/200



Annular Phantom Contrast - 150/150/175

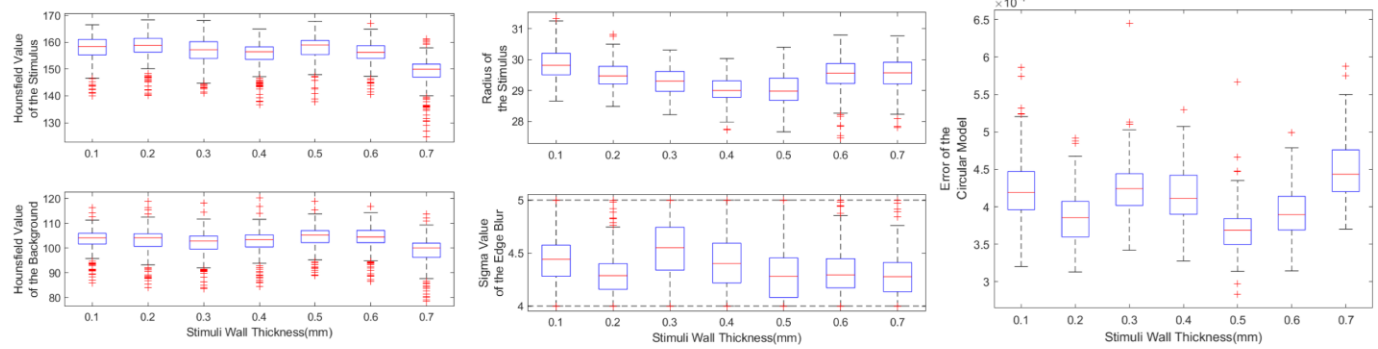


Figure 34. Box plots of the modeling result

5.4 Spiculated Phantom

5.4.1 Clinical Significance of the Spiculated Phantom

Spiculation, where the margin of the nodule has zigzag contour, can be a sign of malignant tumor that is resulted from the scarring of the lung interstitium at the lesion site. For example, the high-resolution CT scan of adenocarcinoma shows spiculated nodule with multiple pleural tails. However, the sign of spiculation could also come from a benign inflammatory process. Appearance of spiculation that's not spiculation could occur in lipoid pneumonia, focal atelectasis, tuberculoma, and progressive massive fibrosis. Again, 3D-printing offers an opportunity to produce spiculated phantom to look at the ability of a CT scanner to reproduce spiculations.

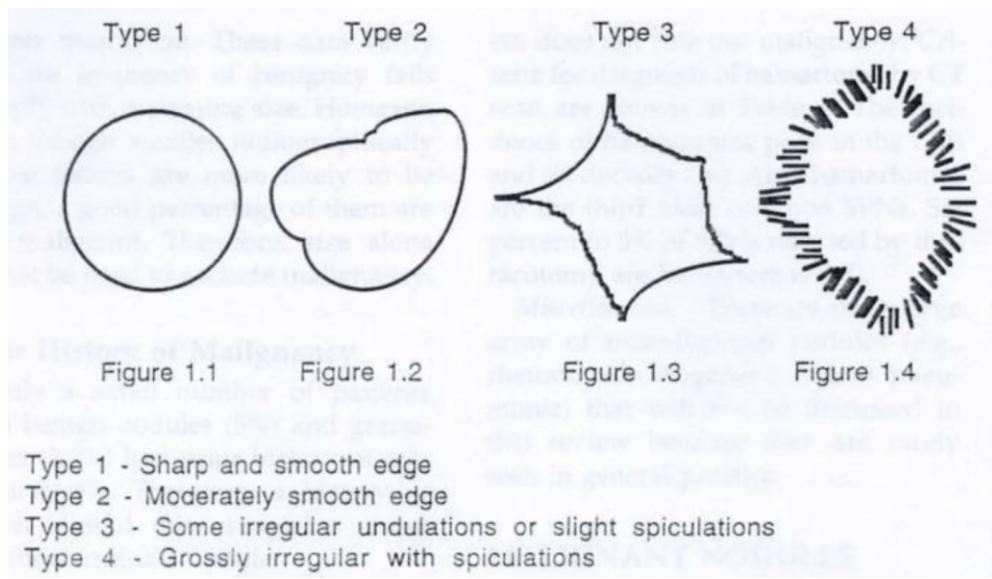
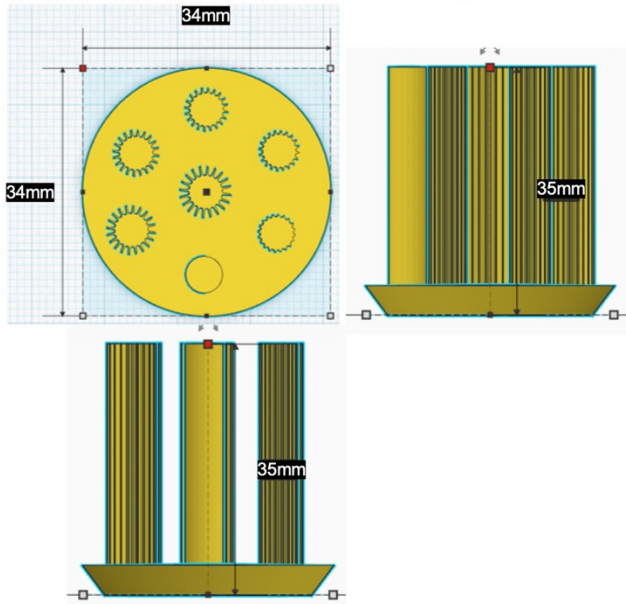


Figure 35. Patterns of Margin. The type 1 to type 4 shows the trend from benign to malignant. The more eccentric the shape, the more malignant the nodule is (Kurian et.al., 2019).

5.4.2 Design of the Spiculated Phantom

Similar to the annular phantom, the spiculated phantom (figure 34) has a varied margin with intruding spike-like edges that resemble the uneven shape of a malignant tumor. We designed the spiculated phantom such that the edge varies from smooth to rough.

Orthographic Projection



Perspective View

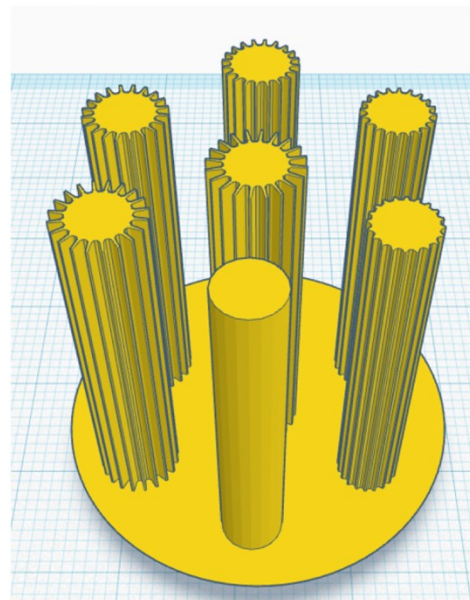


Figure 36. Schematics of the design of the spiculated phantom

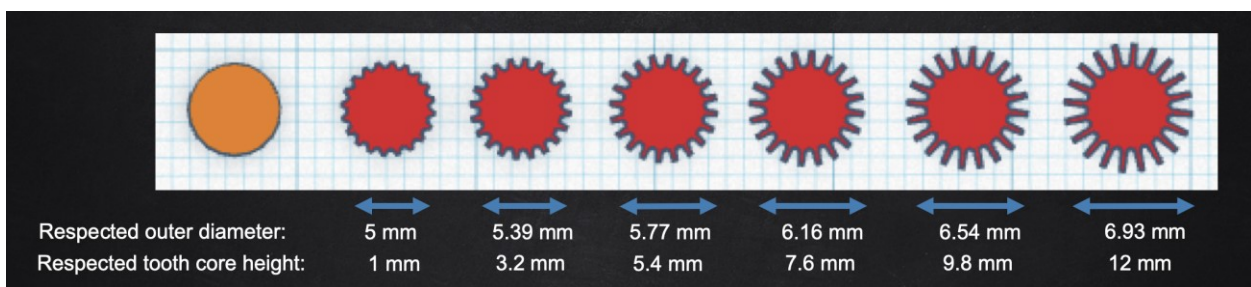


Figure 37. Parameters for the specific design

5.4.3 CT Scan of the Spiculated Phantom

We have immersed the spiculated phantom in water and scanning according to standard protocols. The reconstructed CT image is shown in figure 36. The variable margins are evident from smooth to more spike-like in the scan illustrating the basic potential of such 3D-printed targets. Future work will consider quantitative measures of spicularity as an imaging metric.

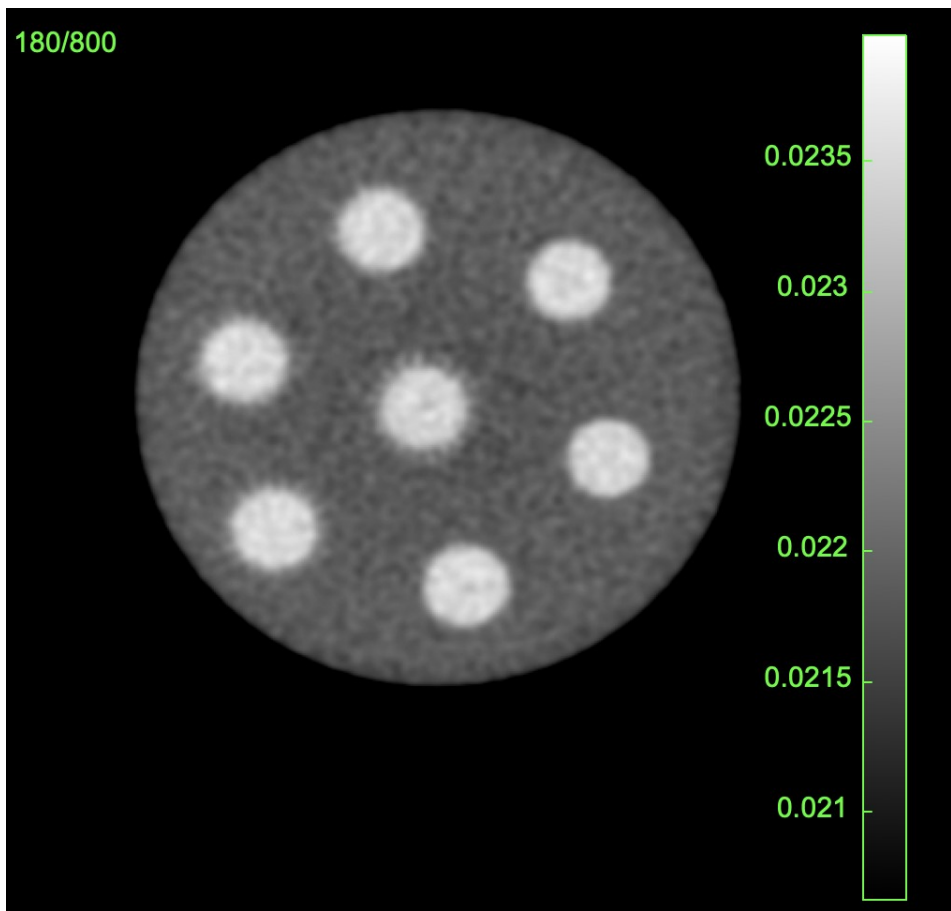


Figure 38. CT image of the spiculated phantom

5.5 Discussion and Future Work

We have illustrated the ability of 3D-printers to provide additional phantom targets beyond the texture studies at the previous chapter. Such target included lesion with variable margin including a transition band (annulus) and irregular spiculated boundaries, as well as vascular structure with variable stenosis and overall diameter. All of the targets may be included in larger anthropomorphic phantoms to model realistic noise and scatter. While much additional quantitative analysis is possible for these customized targets, we have presented and demonstrated the fundamental capacity to produce such targets.

REFERENCE

- Ali, R. (n.d.). Easy-to-Understand Computed Tomography by rehmanali1994. Retrieved December 11, 2019, from https://rehmanali1994.github.io/easy_computed_tomography.github.io/
- Altenbernd, J., Heusner, T. A., Ringelstein, A., Ladd, S. C., Forsting, M., & Antoch, G. (2011). Dual-energy-CT of hypervasculär liver lesions in patients with HCC: investigation of image quality and sensitivity. *European Radiology*, 21(4), 738–743. <https://doi.org/10.1007/s00330-010-1964-7>
- Baek, J., & Pelc, N. J. (2010). The noise power spectrum in CT with direct fan beam reconstruction. *Medical Physics*, 37(5), 2074–2081. <https://doi.org/10.1118/1.3378673>
- Bamba, J., Araki, K., Endo, A., & Okano, T. (2013). Image quality assessment of three cone beam CT machines using the SEDENTEXCT CT phantom. *Dentomaxillofacial Radiology*, 42(8). <https://doi.org/10.1259/dmfr.20120445>
- Beister, M., Kolditz, D., & Kalender, W. A. (2012). Iterative reconstruction methods in X-ray CT. *Physica Medica*, 28(2), 94–108. <https://doi.org/https://doi.org/10.1016/j.ejmp.2012.01.003>
- Brant, W. E., & Helms, C. A. (1999). *Fundamentals of diagnostic radiology*. Williams & Wilkins.
- Canellas, R., Mehrkhani, F., Patino, M., Kambadakone, A., & Sahani, D. (2016). Characterization of Portal Vein Thrombosis (Neoplastic Versus Bland) on CT Images Using Software-Based Texture Analysis and Thrombus Density (Hounsfield Units). *American Journal of Roentgenology*, 207(5), W81–W87. <https://doi.org/10.2214/AJR.15.15928>
- Chou, R., Cuevas, C., Fu, R., Devine, B., Wasson, N., Ginsburg, A., ... Sullivan, S. (2014). AHRQ Comparative Effectiveness Reviews. In *Imaging Techniques for the Diagnosis and Staging of Hepatocellular Carcinoma*. Rockville (MD): Agency for Healthcare Research and Quality (US).
- CIRS Tissue Simulation & Phantom Technology. (2013). *CBCT IMAGE QUALITY PHANTOM*.
- Cremer, J. T., & Cremer, J. T. (2013). Kirchhoff Equation Solution for CRL, Pinhole, and Phase Contrast Imaging. *Neutron and X-Ray Optics*, 555–659. <https://doi.org/10.1016/B978-0-12-407164-3.00010-3>

- Dolly, S., Chen, H.-C., Anastasio, M., Mutic, S., & Li, H. (2016). Practical considerations for noise power spectra estimation for clinical CT scanners. *Journal of Applied Clinical Medical Physics*, 17(3), 392–407. <https://doi.org/10.1120/jacmp.v17i3.5841>
- Erasmus, J. J., Connolly, J. E., McAdams, H. P., & Roggli, V. L. (2000). Solitary pulmonary nodules: Part I. Morphologic evaluation for differentiation of benign and malignant lesions. *Radiographics*, Vol. 20, pp. 43–58. <https://doi.org/10.1148/radiographics.20.1.g00ja0343>
- Filippou, V., & Tsoumpas, C. (2018). Recent advances on the development of phantoms using 3D printing for imaging with CT, MRI, PET, SPECT, and ultrasound. *Medical Physics*, 45(9), e740–e760. <https://doi.org/10.1002/mp.13058>
- Goldman, L. W. (2007). Principles of CT: Radiation dose and image quality. *Journal of Nuclear Medicine Technology*, 35(4), 213–225. <https://doi.org/10.2967/jnmt.106.037846>
- Gould, M. K., Donington, J., Lynch, W. R., Mazzone, P. J., Midthun, D. E., Naidich, D. P., & Wiener, R. S. (2013). Evaluation of individuals with pulmonary nodules: when is it lung cancer? Diagnosis and management of lung cancer, 3rd ed: American College of Chest Physicians evidence-based clinical practice guidelines. *Chest*, 143(5 Suppl), e93S-e120S. <https://doi.org/10.1378/chest.12-2351>
- Hernandez-Giron, I., den Harder, J. M., Streekstra, G. J., Geleijns, J., & Veldkamp, W. J. H. (2019). Development of a 3D printed anthropomorphic lung phantom for image quality assessment in CT. *Physica Medica: European Journal of Medical Physics*, 57, 47–57. <https://doi.org/10.1016/j.ejmp.2018.11.015>
- Hsieh, J. (2015). *Computed Tomography: Principles, Design, Artifacts, and Recent Advances* (Third Edit). John Wiley & Sons, Ltd.
- Jacobs, P. F. (1993). *Rapid Prototyping and Manufacturing: Fundamentals of StereoLithography*. New York, NY, USA: McGraw-Hill, Inc.
- Kikano, G., A, F., & R, S. (2015). Evaluation of the Solitary Pulmonary Nodule. *American Family Physician*, 92(12)(Dec 15), 1084-1091A. Retrieved from <https://www.aafp.org/afp/2015/1215/p1084.html>
- Kurian, T. (n.d.). Solitary Pulmonary Nodule. Retrieved December 3, 2019, from <https://www.slideshare.net/thomaskurian7923/solitary-pulmonary-nodule-55307859/33>
- Kyoto Kagaku CO. LTD. (n.d.). Multipurpose Chest Phantom N1 “Lungman.” Retrieved December 12, 2019, from https://www.kyotokagaku.com/lineup/pdf/ph-1_catalog.pdf
- Leef, J. L., & Klein, J. S. (2002). The solitary pulmonary nodule. *Radiologic Clinics of North America*, 40(1), 123–143, ix. [https://doi.org/10.1016/s0033-8389\(03\)00113-1](https://doi.org/10.1016/s0033-8389(03)00113-1)

- Lin, E., & Alessio, A. (2009). What are the basic concepts of temporal, contrast, and spatial resolution in cardiac CT? *Journal of Cardiovascular Computed Tomography*, 3(6), 403–408. <https://doi.org/10.1016/j.jcct.2009.07.003>
- Lubner, M. G., Smith, A. D., Sandrasegaran, K., Sahani, D. V., & Pickhardt, P. J. (2017). CT Texture Analysis: Definitions, Applications, Biologic Correlates, and Challenges. *RadioGraphics*, 37(5), 1483–1503. <https://doi.org/10.1148/rg.2017170056>
- Mahesh, M. (2002). The AAPM/RSNA physics tutorial for residents: Search for isotropic resolution in CT from conventional through multiple-row detector. *Radiographics*, 22(4), 949–962. <https://doi.org/10.1148/radiographics.22.4.g02jl14949>
- Meeson, S., Turnbull, S. D., & Golding, S. J. (2017). Design of a novel soft tissue-mimicking phantom with randomizable low contrast features for use in CT and MRI. *Biomedical Physics and Engineering Express*, 3(6). <https://doi.org/10.1088/2057-1976/aa896c>
- MIDTHUN, D. E., SWENSEN, S. J., & JETT, J. R. (1993). Approach to the Solitary Pulmonary Nodule. *Mayo Clinic Proceedings*, 68(4), 378–385. [https://doi.org/10.1016/S0025-6196\(12\)60136-0](https://doi.org/10.1016/S0025-6196(12)60136-0)
- Miracle, A. C., & Mukherji, S. K. (2009, June). Conebeam CT of the head and neck, part 1: Physical principles. *American Journal of Neuroradiology*, Vol. 30, pp. 1088–1095. <https://doi.org/10.3174/ajnr.A1653>
- Miracle, A. C., & Mukherji, S. K. (2009, August). Conebeam CT of the head and neck, part 2: Clinical applications. *American Journal of Neuroradiology*, Vol. 30, pp. 1285–1292. <https://doi.org/10.3174/ajnr.A1654>
- Murata, K., & Nitta, N. (n.d.). Multipurpose Chest Phantom Kyoto Kagaku N1 “LUNGMAN” sold by Supertech kyotokagaku. Retrieved December 12, 2019, from 2019 website: <https://www.supertechx-ray.com/Anthropomorphic/X-RayRadiography/KyotoLUNGMAN.php>
- Murata, S., Niggemann, P., Lee, E. W., & Hol, P. K. (2015). Diagnostic and interventional radiology for liver diseases. *BioMed Research International*, Vol. 2015. <https://doi.org/10.1155/2015/147583>
- Ota, H., Takase, K., Rikimaru, H., Tsuboi, M., Yamada, T., Sato, A., ... Takahashi, S. (2005). Quantitative Vascular Measurements in Arterial Occlusive Disease. *RadioGraphics*, 25(5), 1141–1158. <https://doi.org/10.1148/rg.255055014>
- Pelletier, G., Ducreux, M., Gay, F., Luboinski, M., Hagège, H., Thong, D., ... Roche, A. (1998). Treatment of unresectable hepatocellular carcinoma with lipiodol chemoembolization: a multicenter randomized trial. *Journal of Hepatology*, 29(1), 129–134. [https://doi.org/https://doi.org/10.1016/S0168-8278\(98\)80187-6](https://doi.org/https://doi.org/10.1016/S0168-8278(98)80187-6)

- Peteya, J. A. (n.d.). Resolving Details of the Nonbiomineralized Anatomy of Trilobites Using Computed Tomographic Imaging Techniques. Retrieved December 12, 2019, from https://www.researchgate.net/publication/319968280_Resolving_Details_of_the_Nonbiomineralized_Anatomy_of_Trilobites_Using_Computed_Tomographic_Imaging_Techniques
- Prince, J., & Links, J. (2015). *Medical Imaging Signals and Systems*. Pearson.
- Randall, K. (2015). *Physics for Scientists and Engineers* (Forth Edit). Pearson.
- Ritman, E. L. (2004). Micro-Computed Tomography—Current Status and Developments. *Annual Review of Biomedical Engineering*, 6(1), 185–208. <https://doi.org/10.1146/annurev.bioeng.6.040803.140130>
- Samuels, O. B., Joseph, G. J., Lynn, M. J., Smith, H. A., & Chimowitz, M. I. (2000). A Standardized Method for Measuring Intracranial Arterial Stenosis. *American Journal of Neuroradiology*, 21(4), 643 LP – 646. Retrieved from <http://www.ajnr.org/content/21/4/643.abstract>
- Schwartz, J. (2001). Calculating Percent Stenosis. *American Journal of Neuroradiology*, 22(1), 228 LP – 228. Retrieved from <http://www.ajnr.org/content/22/1/228.abstract>
- Sharma, K. V., Gould, J. E., Harbour, J. W., Linette, G. P., Pilgram, T. K., Dayani, P. N., & Brown, D. B. (2008). Hepatic Arterial Chemoembolization for Management of Metastatic Melanoma. *American Journal of Roentgenology*, 190(1), 99–104. <https://doi.org/10.2214/AJR.07.2675>
- Stayman, J. W., Dang, H., Ding, Y., & Siewerdsen, J. H. (2013). PIRPLE: a penalized-likelihood framework for incorporation of prior images in CT reconstruction. *Physics in Medicine and Biology*, 58(21), 7563–7582. <https://doi.org/10.1088/0031-9155/58/21/7563>
- UCSF. (n.d.). Hepatic Artery Embolization. Retrieved from <https://general.surgery.ucsf.edu/conditions--procedures/hepatic-artery-embolization.aspx>
- University of Wisconsin. (n.d.). Interactions of Gammas. Retrieved December 11, 2019, from https://pages.hep.wisc.edu/~prepost/407/gamma/gamma_html.html
- Vilgrain, V., Lagadec, M., & Ronot, M. (2016). Pitfalls in Liver Imaging. *Radiology*, 278(1), 34–51. <https://doi.org/10.1148/radiol.2015142576>
- Yuksel, M., Demirpolat, G., Sever, A., Bakaris, S., Bulbuloglu, E., & Elmas, N. (2007). Hydatid disease involving some rare locations in the body: A pictorial essay. *Korean Journal of Radiology*, 8(6), 531–540. <https://doi.org/10.3348/kjr.2007.8.6.531>
- Zeman, R. K., Fox, S. H., Silverman, P. M., Davros, W. J., Carter, L. M., Griego, D., ... Cooper1, C. J. (1993). Helical (Spiral) CT of the Abdomen Review Article. In *AJR* (Vol. 160). Retrieved from www.ajronline.org

Solitary Pulmonary Nodule. (n.d.). Retrieved December 1, 2019, from
<https://www.slideshare.net/thomaskurian7923/solitary-pulmonary-nodule-55307859/33>

PHANTOMS FOR PERFORMANCE EVALUATION AND QUALITY ASSURANCE OF CT SCANNERS American Association of Physicists in Medicine. (1977).

HUI “AMALIE” SHI

245 West 31st Street, Baltimore, MD 21211

huishi@jhmi.edu 443-240-3700

EDUCATION

JOHNS HOPKINS UNIVERSITY, Whiting School of Engineering, Baltimore, Maryland

Master of Science in Biomedical Engineering: December 2019

GEORGIA INSTITUTE OF TECHNOLOGY, Atlanta, Georgia

Bachelor of Science in Biomedical Engineering with Highest Honors: December 2016 **GPA:** 3.64

RESEARCH EXPERIENCE

JOHNS HOPKINS UNIVERSITY, Baltimore, MD

- Medical Image Analyst**, Advanced Imaging Algorithms & Instrumentation Lab *April 2018 - Dec 2019*
- Designed 3D-printed vascular stenosis, liver, and lung nodule CT target with Solidworks, MATLAB, and AutoCAD.
 - Molded and cast anthropomorphic phantoms and spherical targets for CT image quality assessment.
 - Segmented / Classified volumetric data using radiomics features (GLCM), power spectral density, filtering, denoising, edge detection, optimization, and clustering to extract & characterize features of the CT image targets with MATLAB.

Graduate Research Assistant, Myocarditis Lab *January 2018 - April 2018*

- Programmed ANCOVA with MATLAB to prove the significance of a hypothesis-driven clinical data sets
- Annotated human heart samples with a high-resolution microscope and characterized the distribution of cardiac cells and invading autoimmune cells.
- Administered therapeutic agents through different routes; performed survival animal surgeries in creating heart failure and cardiac arrest models in mice/rats (intubation/mechanical ventilation and arterial/vein cannulation).
- Harvested heart and spleen and cultured cell in vitro; purified and isolated cells and prepared the histology sample of the heart; performed molecular biology experiments such as real-time PCR, ELISA, flow cytometry, Western Blot, and immunostaining.

GEORGIA INSTITUTE OF TECHNOLOGY, Atlanta, GA

Biological Signal Data Analyst, Neuro-electrophysiology Lab *September 2013 - July 2017*

- Engineered a feedback-controlled implanted stimulation system to reduce foot drop symptom by electrically stimulating the muscle through intramuscular electrodes.
- Applied linear quadratic regulator theory (MATLAB) and NEUROMECHANIC to simulate the stretch of a muscle to predict the response of another muscle.

Biomechanical Test Engineer, Quantitative Physiology Lab *Fall 2014*

- Dissected Northern Leopard Frog, identified sciatic nerve, separated gastrocnemius muscle, measured isometric force versus muscle length.
- Dissected pig heart along with real time ECG reading analysis with written LABVIEW program.
- Mechanical testing to measure effects of sterilization on surgical gloves according to ASTM standards.

CONFERENCES, PUBLICATIONS AND AWARDS

[P]. Shi, H., Gang, G., Li, J., Liapi, E., Abbey, C., Stayman, JW., *Performance Assessment of Texture Reproduction in High-Resolution CT*, SPIE 2020 conference proceeding

[C]. Shi, H., Lyle, M., Turtill, C., Nichols, R., *Positive force feedback may ameliorate muscle weakness*, 2017 SfN's 47th annual meeting poster

[C]. Lyle, M., Shi, H., Anderson, H., Rapsas, B., Nichols, R., *Behavioral adaptations during downslope walking after cross-reinnervation of medial gastrocnemius and the pretibial flexors*, 2017 SfN's 47th annual meeting poster

[C]. Li, J., Gang, G., Shi, H., Stayman, JW., *3D-printed Texture Phantoms for Assessment of High-Resolution CT*, AAPM 2019 annual meeting presentation

HUI “AMALIE” SHI

WORK EXPERIENCE

- Consultant** JOHNS HOPKINS UNIVERSITY, Study Consulting Program *Fall 2017*
• Mentored three undergraduate students weekly to help develop better study habits.
- Head Mathematics Teaching Assistant** GEORGIA INSTITUTE OF TECHNOLOGY *Fall 2014 – Fall 2016*
• Led 20 students in two 50-minute recitation sessions each week to reinforce Calculus I concepts.
• Graded papers and held office hours to answer homework and exam questions.
• Communicated with students and the course instructor to improve classroom learning.
- Genetic Intern** BGI GROUP *Summer 2014*
• Performed basic genetic experiments such as PCR and gel electrophoresis.
• Led a team of 15 students in debates and discussions in genetic research, big data research and bio-ethical issues.

LEADERSHIP EXPERIENCE

- Vice President:** Georgia Tech Women’s Chorus *Fall 2012 – Fall 2015*
- Secretary:** Biomedical Research Opportunities Society *Fall 2012 – Fall 2014*
- Staff Writer:** Pioneer BME Publication *Spring 2013 – Spring 2014*

RELEVANT SKILLS

- Biomedical Engineering Design and Problem Solving:** Medical Device Design Communication (drawing, modeling, CAD), FDA Quality System Regulations
- Software:** MATLAB, Simulink, SolidWorks, R, Python, LabVIEW, Illustrator, EndNote, LaTeX, ChemBioDraw
- Statistics, Computational Modeling and Applications:** Statistics and Probability, Simulation of Biomedical Scenarios, Dynamical System Modeling, Design of Systems Models, Parameter Estimation, Phase-plane Analysis, Optimization
- Instrumentation:** Oscilloscope, Function Generator, Digital Multimeter, NI myDAQ
- Communication:** IRB Applications, Patent Applications, Technical Document Writing (R21 Project Proposal, Technical Report)